國 立 中 央 大 學

大 氣 科 學 學 系

碩 士 論 文

使用 Morrison 方案和雙偏極化雷達進行中尺度對流系統雲物理特性上的模擬和驗證

Simulation and Validation of the MCS Microphysical Characteristics using Morrison Two-Moment Scheme and Dual-Polarimetric Radar

研 究 生：楊詠荃

指導教授：張偉裕 博士

中 華 民 國 一 一 零 年 六 月

國立中央大學圖書館學位論文授權書

填單日期：110 / 09 / 06

2019.9 版

授權人姓名	楊詠荃	學 號	108621018
系所名稱	大氣物理所	學位類別	☑碩士 □博士
論文名稱	使用 Morrison 方案和雙偏極化雷達進行中尺度對流系統雲物理特性上的模擬和驗證	指導教授	張偉裕

學位論文網路公開授權

授權本人撰寫之學位論文全文電子檔：

・在「**國立中央大學圖書館博碩士論文系統**」.

(V)同意立即網路公開

( )同意 於西元______年______月______日網路公開

( )不同意網路公開，原因是：______

・在國家圖書館「**臺灣博碩士論文知識加值系統**」

(V)同意立即網路公開

( )同意 於西元______年______月______日網路公開

( )不同意網路公開，原因是：______

依著作權法規定，非專屬、無償授權國立中央大學、台灣聯合大學系統與國家圖書館，不限地域、時間與次數，以文件、錄影帶、錄音帶、光碟、微縮、數位化或其他方式將上列授權標的基於非營利目的進行重製。

學位論文紙本延後公開申請 (紙本學位論文立即公開者此欄免填)

本人撰寫之學位論文紙本因以下原因將延後公開

・**延後原因**

( )已申請專利並檢附證明，專利申請案號：

( )準備以上列論文投稿期刊

( )涉國家機密

( )依法不得提供，請說明：______

・**公開日期**：西元______年______月______日

※繳交教務處註冊組之紙本論文(送繳國家圖書館)若不立即公開，請加填「國家圖書館學位論文延後公開申請書」

研究生簽名：楊詠荃　　　指導教授簽名：張偉裕

Abstract

Compared to warm-rain processes which is well understood in decades of advancement, cold-rain microphysics of precipitation is still challenging task in numerical model simulation. The deficient knowledge in cold–rain processes may result in incorrect ice-phased drop size distribution (DSD) of various hydrometers simulated in microphysics scheme. Past studies have proven the inseparable relationship between polarimetric variables and storm microphysics. In the research, Morrison two moment scheme which is a double-moment (DM) scheme is selected to simulate a MCS located at southwest Taiwan on 14 June 2008 (SoWMEX-IOP8). The simulation is validated quantitatively with the NCAR s-band polarimetric measurements and DSD retrievals of raindrops and snow particles. Simulation results from Morrison scheme are found overestimating the reflectivity (Z_{HH}) comparing to observation. The analysis reveals that stronger Z_{HH} is due to the exaggerated mean snow particle sizes (mass-weighted diameter, $D_m > 0.7$ mm), even though model underestimates the snow mixing ratio (q). The increments of mixing ratio and D_m of snow particle which contributed from different cold-rain microphysical processes are analyzed. The autoconversion of graupel from cloud-riming snow is one of the dominating processes. Two sensitivity experiments including snow concentration and coefficient of collection efficiency of snow for cloud (eci) were performed. The results indicate only slightly improvements of the simulated snow DSD.

摘要

相較於暖雨雲物理過程的研究在過去取得很大成就，冷雨過程在大氣數值模擬仍是很大挑戰。對冷雨過程的無知很有可能會造成雲物理方案在冰相粒子粒徑分布(DSD)上的模擬錯誤。過去許多研究已經證明偏極化雷達變數和雲物理之間緊密的關係。本篇研究使用 Morrison 這個雙矩量雲物理方案模擬二零零八年六月十四號台灣西南的中尺度對流系統(SoWMEX-IOP8)。模擬的結果會以 NCAR S-band 雷達的偏極化觀測以及其雪(snow)和雨(rain)的粒徑分布反演來驗證。

Morrison 方案模擬的回波(Z_{HH})被發現高估了觀測。分析發現，這起因於 Morrison 方案產生了過大粒徑(質量權重粒徑 D_m>0.7mm)的雪。因此即使在低估了雪的混和比(q)情況下，模擬仍能產生更強的回波。在接下來的部分，本文討論不同冷雨過程對雪的混和比以及質量權重粒徑增量的貢獻。發現受雲滴霜化的雪(cloud-riming snow)轉換(auto-convert)成冰霰(graupel)這個過程與其他冷雨過程相比在粒徑增量上占很重要的腳色。接著針對雪的數目濃度(number concentration)和雪對雲滴(cloud)的收集效率係數(eci)設計與實行兩組敏感度測試。而結果顯示，這些測試對雪的粒徑分布模擬改善非常輕微，這暗示了微物理過程很有可能不是最主要的過程。

Acknowledgment

這段時間不管是做研究還是寫論文都進行得很倉促，許多工具是上手沒多久就馬上要正確的使用。我想我的碩士研究能順利在時限內完成，很重要的原因是在碩一打下的基礎。包括張偉裕老師開的相關課程，以及反覆多次 T-matrix 模擬的練習。此外，那時與張老師進行的雪密度估測研究也是很好的訓練。當然，系上碩士書報課以及氣象局天氣分析研討會等等提供了我許多的上台臨場經驗。另外，實驗室的老師們也給予我研究上許多寶貴建議。還有謝謝三位口委在口試時指出了我研究上許多的盲點，包含論文敘述的架構以及研究本身的設計，這些確實都是我思慮不周而沒發現的。也謝謝身邊的同學還有我的室友常常聽我講一些無聊的話來平衡偶爾研究上時的煩悶。最後要謝謝我的父母，讓我在經濟無虞的情況下完成碩士研究。

Outline

Figures

Chapter 1: Introduction

Cloud microphysics is a critical factor in atmosphere science. The cloud microphysics consists two main parts: warm-rain and cold-rain processes. Warm-rain processes contain the development of precipitating rain without the ice-phased particles. Cold-rain processes, on the other hand, focus on the ice-phase microphysics (Straka 2009). Compared to warm-rain processes which is well understood in decades of advancement (Kessler 1969; Berry and Reinhardt 1974; Ziegler 1985; Cohard and Pinty 2000; Morrison and Grabowski 2007), numerical simulations of various cold-rain processes are still challenging to atmospheric science community. The cold-rain processes are difficult to be formulated in numerical model due to inherent complexity of ice-phased hydrometeor (Morrison and Grabowski 2008). Furthermore, cold-rain microphysics play an important role in deep convection. The concentration and mass of ice-phased particles are significantly affected by different cold-rain processes. For example, aggregation of snow decreases snow number concentration yet the auto-conversion from ice to snow increases the concentration. Hence, the aggregation of snow and auto-conversion from ice to snow processes are considered as sink and source of snow concentration, respectively. Deviation in the source or sink of ice-phased variables can led to inaccurate concentration, mass flux, and so on. As the incorrect ice-phased particle simulated by numerical model above the melting layer, this error consequently propagates to the warm-rain process beneath melting layer (Chen 2018). It is essential to simulated proper characteristics of ice-phased particles above 0-degree isotherm.

Seldom observational data can provide detail of microphysical characteristics with high spatiotemporal resolution, especially above freezing level. Numerical simulation, on the other hand, can provide adequate spatiotemporal resolutions results. Yet, simulation is still suffered from insufficient spatial resolution. Numerical mode simulation still contains many uncertainties due to deficient understanding of microphysics. Therefore, the imperfect numerical solutions are validated with appropriate observations for further improvements. A consistent performance of simulation with observation ensures the fidelity of numerical model result. Nonetheless, contradiction between simulation and observation reveals the shortcoming of numerical model and provides a chance to advance the formula and parameters of microphysical schemes in numerical model.

In numerical model, microphysics parameterization scheme responses for physics process in micro scale. That is, the warm-rain and cold-rain process. The capability of microphysical scheme to illustrate nature characteristic is a significant task. Validation must be conduct to understand if the microphysical scheme be handled properly. Since microphysics variables show high spatial variability, radar observations of RHI scan with high resolution is suitable for comparison. Also, past researches have proven polarimetric radar data can better reveal the storm microphysical processes (Johnson et al. 2016). The inseparable relationships between radar observations and microphysical properties justify the validation of microphysical scheme with polarimetric variables. Specific spatial pattern of polarimetric variables, namely polarimetric radar signature, are corresponding to particular signature of microphysical processes. For example, size sorting effect of large size of raindrops fall faster to surface, thus higher values of Z_{DR} can be found near surface. In the perspective of simulation, reproducing these signatures exhibits that the model and microphysical scheme can reconstruct both storm dynamics and microphysics properly (Johnson et al. 2016). In short, polarimetric radar observations provide key information of microphysical processes. Furthermore, the signatures of polarimetric radar observations serve as the basis to understand whether particular parameterization scheme correctly treats the associated cloud microphysical processes.

Microphysical features of various type of particle include the drop size distribution (DSD), density, shape, orientation of particles and falling behavior (e.g., caning angle). Polarimetric radar observations are highly associated with these features and hence can be used to examine the microphysics parameterization scheme. However, numerical model cannot simulate polarimetric variable directly. The polarimetric variables need to be simulated from prognostic variables of model with the polarimetric operator. Validations not only can be conducted on polarimetric variables, but also can be conducted on the DSD parameters. Retrieval schemes enable revealing the DSD parameters from polarimetric measurements. In microphysics parameterization scheme, microphysical processes increase or decrease the number concentration (Nt) and mixing ratio of each hydrometeor species. The number concentration and mixing ratio, deeply affected by these processes, corresponding to specified DSD. Therefore, the validation of simulated DSD parameters provides alternative approach to directly examine the simulated microphysical processes of microphysics scheme.

Among many bulk microphysical schemes, Morrison two moment scheme is one of the few that simulates both the mixing ratios and number concentrations of ice, snow, rain, and graupel. Since both number concentration and mixing ratios of hydrometeor species evolve as a result of microphysical processes, Morrison scheme show higher potential to better handle microphysical processes than those which only simulate mass mixing ratio. Also, Johnson et al. (2016) and Morrison et al. (2009) have proven that microphysical schemes which predict both number concentration and mixing ratio (double moment scheme, DM) perform better than those only predict mixing ratio (single moment scheme, SM). Morrison scheme should be more capable in microphysical simulation theoretically; however, the fact is not as expected in all studies. Yu (2019) compared the performance of microphysics schemes including Goddard, WSM6, WDM6, and Morrison with polarimetric operator during Southwest Monsoon Experiment intensive observing period 8 (SoWMEX IOP8). In the validation of Z_{HH} and Z_{DR}, SM scheme such as Goddard and WSM6 perform better than Morrison and WDM6, that is, the DM scheme. Therefore, detail examination and understanding of Morrison scheme simulation is required, especially the cold-rain microphysics which is not focused in Yu (2019).

In the study, simulation of the mesoscale convective system (MCS) in southwest Taiwan on 14 June 2008 (SoWMEX IOP8) is validated with the NCAR S-band polarimetric radar (SPOL) radar data. Morrison scheme with double moment is chosen to reconstruct the microphysical processes via WRF simulation. Besides, high spatiotemporal resolution data of RHI scans from NCAR SPOL polarimetric radar is applied for validation. The polarimetric variables observed are highly related to microphysical condition and are regarded as the reference truth to examine the performance of Morrison scheme. Also, retrievals of polarimetric variables provide a more intuitive validation to the simulated DSD. Finally, two sensitive experiments toward microphysical processes are designed in attempt to improve the simulation.

Chapter 2: Case and data

2.1 Case overview

The MCS case chosen in the study is a prefrontal squall line on 14 June 2008 which is the first day of the SoWMEX IOP8(14-17 June). The MCS observed by NCAR SPOL radar propagated from southeast China and exhibit northeast-southwest line pattern before landing on the southwest coast of Taiwan (Fig. 2.1).

In synoptic overview, a quasi-stationary mei-yu front is near Taiwan. Also, the 500-hPa trough and 850-hPa cyclone cause strong low- to middle-level southwest flow (Xu et al. 2012). According to Davis and Lee (2012), the northerly and northeasterly in the lowest 50-hPa veered into southwesterly flow at 850-hPa imply the warm-advection that assist the development of the MCS. Xu and Zipser (2015) found the precipitation from the MCS was stronger than other cases during SoWMEX experiment. Moreover, from the pronounced radar reflectivity around the melting layer, vigorous cold-rain microphysics processes and significant updraft must exist in the MCS on 14 June.

2.2 Sounding data

The sounding data of 14 June were collected by several ground-based stations of Taiwan (Fig. 2.2). The time interval between each launch are about 3 hours; therefore, there were 8 sounding per day. Sounding of Pingtung station which is the nearest station to SPOL radar are used in the study. All of the sounding data were processed by Paul et al. (2010) to remove bias. The data were then interpolated into 0.25 km interval from surface to 10 km height. Variables such as temperature and air density are calculated for determining melting layer height and retrieving microphysics characteristic from dual-polarimetric radar variables.

2.3 Radar data

2.3.1 RHI strategy

In order to obtain detail information of storm microphysics, radar data with range-height-indicator (RHI) are investigated. The RHI measurements analyzed in the study are NCAR SPOL. Observational variables like reflectivity factor at horizontal polarization (Z_{HH}), differential reflectivity (Z_{DR}), and specific differential phase (K_{DP}) provided by the SPOL radar are regarded as reference truth to examine the simulation from model. These variables and other dual-polarimetric variables are introduced detail in Appendix (A.1). From 0736 to 0913 UTC is the only valid period of consecutive RHI scans from SPOL radar on 14 June. The time interval between each set of RHI scans are about 6 to 23 minutes. Each set includes 8 to 11 RHI scans and the azimuthal angle of them range from 11 to 40 degree, that is, the northeast of the SPOL radar.

2.3.1 Radar data processing

In the quality control, the data with LDR over than 0.0 dB or ρ_{HV} less than 0.5 are removed. After removing the non-meteorological data, the data are interpolated into a two-dimension domain (x-z coordinate). The vertical dimension of the domain ranges from 0 to 10 km height with the interval equal 0.25 km. On the other hand, the horizontal dimension ranges from 10 to 60 km to radar center with the 0.25 km interval. The data of SPOL radar are available from 0 to over 100 km range distance. However, to avoid the beam smoothing problem, only data with range distance less than 60 km are analyzed in the study. The interpolation follows the algorithm:

$$var(x,z) = \frac{\sum_{i=1}^{i=N} w(d_i)var_i}{\sum_{i=1}^{i=N} w(d_i)} \qquad (2.1)$$

$$w(d_i) = \frac{1}{{d_i}^4} \qquad (2.2)$$

var can be Z_{HH}, Z_{DR}, or K_{DP}. d_i is the distance from the *ith* grid point to the location of interpolation point. var_i is the value of *ith* grid point. Weight (*w*) of interpolation is selected to be the inverse distance to the fourth power ($1/{d_i}^4$). This weight is designed to ensures retaining the texture of weather system. Profile of Z_{HH} (x-z coordinate) before (left) and after (right) the interpolation are demonstrated in Figure 2.3. It illustrate that the interpolated data is similar to original RHI scan.

Chapter 3: WRF simulation

3.1 Model setup

The Weather Research and Forecasting (WRF) Model is the numerical model for weather simulation and prediction. In this study, the fully compressible and non-hydrostatic model of version 4.2.1 is used for the simulation. Numerical model handles physics of different scales of weather systems, and as the grid resolution increases, microphysics that can be directly represented in model grids. That is, the model allows the cloud development and evolution by including the explicit equations of interactions and transitions of different hydrometeor species (Stensrud 2007). The grid spacing in the simulation of this study are 9, 3, and 1 km corresponding to 421×421, 451×451, and 430×521 grid points for the three nested domains assumed (Fig. 3.1). Also, the vertical dimension has 49 layers to ensure sufficient resolution resolving the signatures around the melting layer. Therefore, it is suitable to apply microphysics scheme in all domains. Morrison two moment scheme is chosen in the study to simulate microphysical processes in three domains.

In the study, the simulation starts from 1800 UTC 13 and stop at 1700 UTC on 14 June 2008. The initial and boundary conditions are from NCEP final analysis (GFS-FNL). The spatial and temporal resolution of GFS-FNL are 1 degree and 6 hours respectively. The entire simulation was constructed from three run with time step equal 15, 10, and 15 secs for the biggest domain (Fig. 3.2) to save computational time. Finally, the analysis in the simulation will focus in the period from 1030 to 1400 UTC during which the MCS happens.

3.2 Microphysics scheme

Microphysics scheme in model is responsible for the evolution of drop size distribution (DSD) and the associated dynamics and thermodynamics in micro-scale. According to different treatment toward DSD, parameterization of microphysics can be done by two methods: bin model and bulk model. Bin model calculates the DSD explicitly, on the other hand, bulk model represents the DSD with a prescribed distribution. For example, Morrison two moment scheme with bulk method assumes exponential distribution for rain, ice, snow, and graupel species. The simplification of the DSD led to less computational cost (Morrison et al. 2005). Morrison two moment scheme utilizes an exponential DSD with two factors: n_0 and λ.

$$\mathrm{n}(D) = n_0 \times e^{-\lambda D} \qquad (3.1)$$

n_0 is the intercept parameter and λ is the slope parameter. D is the diameter of particle. n is the number concentration of particles in diameter D. Besides the n_0 and λ, one can derive the DSD from mixing ratio (q) and total number concentration (n_t) under exponential assumption. In fact, the convert formula enables transforming parameters from n_0 and λ to q and n_t and vice versa:

$$\mathrm{q} = \pi \rho_x \frac{n_0}{\lambda^4 \rho_{air}} \qquad (3.2)$$

$$n_t = \frac{n_0}{\lambda} \qquad (3.3)$$

In Morrison two moment scheme, prognostic equations simulate q and n_t at each time step at each grid point in the domain. There are two variables q and n_t needed to determine the DSD time evolution and spatial variation; thus, Morrison scheme is called the double moment scheme (DM). In contrast, single moment scheme (SM) determine the DSD by only one prognostic variables. Although SM scheme consumes less computational resources, it is limited in represent the variation of DSD in atmosphere compared to the DM scheme in theory.

Chapter 4: Methodology

The validation of simulations rely on the polarimetric radar observations; however, the observational variables are fundamentally different from the microphysical variables simulated in model. Prognostic variables associated with microphysics in model are mixing ratio (q) and total number concentration (n_t) of each species. The model variables q and n_t describe the integrated mass and number on the drop size distribution (DSD) respectively. On the other hand, observed variables such as Z_{HH}, Z_{DR}, and K_{DP} are associated with the signal received by radar and are dependent on various microphysical conditions. Hence, the model variables cannot be compared directly with the measurements. In order to quantitatively compare the simulated results to the radar measurements, two methods are carried up in the study: polarimetric operator and DSD retrieval. The former calculates simulated model variables into simulated polarimetric variables; on the contrary, the latter turns the observed polarimetric variables into q, n_t or others parameters of DSD, that is, the “retrieved” model variables. The connation inside the two methods, the former examines simulation on a more general perspective of microphysics, while the latter gives a more intuitive validation on the simulated DSD which is on behalf by q and n_t or others related parameters.

4.1 Polarimetric operator

Polarimetric variables come from the received scattering power and correlations of various radar signals within the radar resolution volume. The radar signal is a collection of ensemble of scattering hydrometeors (Ryzhkov and Zrnic 2019). Therefore, polarimetric variables are highly associated with the hydrometeors size distribution (DSD) in the atmosphere. The algorithm, namely T-matrix method, calculates polarimetric variables from DSD information with prescribed assumptions about hydrometeor characteristics (such as particle density, shape, and orientation). T-matrix method is the numerical solutions of Maxwell's equations which describes the behavior of electromagnetic waves like propagation and backscattering. Also, T-matrix method is still applicable when the Rayleigh approximation fail in the resonance region, (Mishchenko et al. 1996). Although T-matrix method retains wider application, it is costly in computation resources. For the reason, in the study, look-up tables of polarimetric variables includes Z_{HH}, Z_{DR}, and K_{DP} are generated from T-matrix method in advance (Johnson et al. 2016). Therefore, one can find the correct polarimetric variables in tables from the DSD parameters without much computation in the polarimetric operator.

As aforementioned in Chapter 3 (3.1), total number concentration and mixing ratio of various species simulated in Morrison scheme can convert to the DSD parameters (n_0 and λ) at each grid points. Thus, the parameters of DSDs are used as input indexes of look-up tables to find the polarimetric variables in each grid points. The DSD is a significant factor that constitute the polarimetric variables, yet not the only factor. Particle characteristics like shape, orientation, density, phase and so on also play a role in determining the polarimetric variables. For example, hydrometeor shape is related with Z_{DR}, and the dielectric constant which is associated with the hydrometeor phase is positive correlated with Z_{HH}. In the study, several look-up tables of polarimetric variables were generated in advance with T-matrix method according to the species characteristics. Hydrometeors are classified into five species in Morrison scheme; therefore, there are five groups of particles with their own characteristics. Rain are liquid-phase species; therefore, apply the dielectric constant of water. In addition, rain retains the relationship of diameter size D and axis ratio r (Brandess et al. 2002).

$$r = 0.9951 + 0.0251D - 0.03644D^2 + 0.005303D^3 - 0.0002492D^4 \quad (4.1)$$

Axis ratio r is used to described the flatness of particles which is the ratio of minor axis to major axis. On the other hand, snow apply smaller density than the rain cases and the axis ratio of snow is fixed to be 0.75. Also, because of the irregular shape of snow, snow keeps higher standard deviation of canting angle (20 degree) than the rain cases (0 degree). For graupel, standard deviation of canting angle is 60 degree and axis ratio is set to be 0.75 which is the same as snow. As for cloud and ice, their contribution to polarimetric variables are negligible because of their insignificant size for S-Band radar. Thus, characteristics and DSDs of cloud and ice will not be discussed in the content. And the look-up tables of ice and cloud won't be generated as the tables of rain, snow, and graupel. More details about rain, snow, and graupel characteristics description used in the study can be found in Jung et al. (2008).

In the operator of this study, polarimetric variables of rain, snow, and graupel can be found in their look-up tables according to their DSD parameters. Variables output from the polarimetric operator include Z_{HH}, Z_{DR}, and K_{DP} which are constructed from the Z_{HH}, Z_{DR}, and K_{DP} of rain, snow, and graupel respectively.

$$Z_H = 10log_{10}\left(Z_{H,r} + Z_{H,s} + Z_{H,g}\right) \ (dBZ) \quad (4.2)$$

$$Z_{DR} = 10log_{10}\left(\frac{Z_H}{Z_V}\right) = 10log_{10}\left(\frac{Z_{H,r} + Z_{H,s} + Z_{H,g}}{Z_{V,r} + Z_{V,s} + Z_{V,g}}\right) \ (dB) \quad (4.3)$$

$$K_{DP} = K_{DP,r} + K_{DP,s} + K_{DP,g} \quad (4.4)$$

The cloud and ice species in Morrison scheme with small particle size for S-band radar are disregarded for polarimetric variables calculation. Overall, the calculations of Z_{HH}, Z_{DR}, and K_{DP} are valid above the melting layer. However, the calculations fail below the 0-degree isotherm where melting process alerts the characteristics of ice-phased particles. Problems arise when same assumptions of snow and graupel characteristics used above and below the melting layer. Therefore, it is necessary to separate the melting species from the subzero ice-phased species. All species in Morrison scheme exist in pure state; therefore, it is difficult to deal with the change of particle characteristics caused by the melting process.

A compromised solution without modification of Morrison scheme is to include a melting model in the polarimetric operator (Jung et al. 2008). In the application, two additional species: rain-snow (melting snow) and rain-graupel (melting graupel) are introduced in the melting model in the polarimetric operator. Part of the mixing ratio of rain q_r and snow q_s are redistributed into the mixing ratio of rain-snow q_{rs} by the factor F.

$$\mathrm{F} = F_{max}\left[min\left(\frac{q_s}{q_r},\frac{q_r}{q_s}\right)\right]^{0.3} \quad , \qquad F_{max} = 0.5 \qquad (4.5)$$

$$q_{rs} = \mathrm{F}(q_r + q_s) \qquad (4.6)$$

Since the microphysical scheme used in Jung et al. (2008) is SM; therefore, only mixing ratio of rain-snow need to be determined. However, Morrison scheme used in the study predicted both mixing ratio and total number concentration (DM). Therefore, there are two variables need to be determined. In the study, the same distribution factor is applied in both mixing ratio and total number concentration of rain-snow $n_{t,rs}$.

$$n_{t,rs} = \mathrm{F}\left(n_{t,r} + n_{t,s}\right) \qquad (4.7)$$

Also, the total number concentration and mixing ratio of rain-graupel $n_{t,rg}$ and q_{rg} come from part of the total number concentration and mixing ratio of rain and graupel.

$$\mathrm{F} = F_{max}\left[min\left(\frac{q_g}{q_r},\frac{q_r}{q_g}\right)\right]^{0.3} \qquad (4.8)$$

$$q_{rg} = \mathrm{F}(q_r + q_g) \ , \quad n_{t,rg} = \mathrm{F}(n_{t,r} + n_{t,g}) \quad (4.9)$$

The dielectric constant of rain-snow mixture used for T-matrix calculation is determined from the liquid-water fraction of the species f_w.

$$f_w = \frac{Fq_r}{F(q_r + q_s)} = \frac{q_r}{q_r + q_s} \qquad (4.10)$$

The liquid-water fraction of the rain-snow mixture increase from 0 to 1 when snow melts completely after falling through the melting layer. Also, the dielectric constant of rain-graupel mixture comes from the similar water fraction but for melting graupel.

$$f_w = \frac{Fq_r}{F(q_r + q_g)} = \frac{q_r}{q_r + q_g} \qquad (4.11)$$

The assumed characteristics of melting species result in the polarimetric look-up tables of rain-snow and rain-graupel with the T-matrix method. Z_{HH}, Z_{DR}, and K_{DP} of melting species can be found in look-up tables from their DSD parameters derived from their mixing ratio and total number concentration. Finally, the total Z_{HH}, Z_{DR}, and K_{DP} are constructed from the Z_{HH}, Z_{DR}, and K_{DP} of rain, snow, graupel, rain-snow, and rain-graupel.

$$Z_H = 10log_{10}(Z_{H,r} + Z_{H,s} + Z_{H,g} + Z_{H,rs} + Z_{H,rg}) \ (dBZ) \quad (4.12)$$

$$Z_{DR} = 10log_{10}\left(\frac{Z_H}{Z_V}\right) = 10log_{10}\left(\frac{Z_{H,r} + Z_{H,s} + Z_{H,g} + Z_{H,rs} + Z_{H,rg}}{Z_{V,r} + Z_{V,s} + Z_{V,g} + Z_{V,rs} + Z_{V,rg}}\right) \ (dB)(4.13)$$

$$K_{DP} = K_{DP,r} + K_{DP,s} + K_{DP,g} + K_{DP,rs} + K_{DP,rg} \qquad (4.14)$$

Melting process in Morrison scheme happens only when the temperature is higher than 0°C. Therefore, the melting model only works below the 0-degree isotherm in the polarimetric operator. These designs of the melting model generate melting snow and graupel (lower panel of Fig. 4.1) has consist simulation results (upper panel of Fig. 4.1) where snow and graupel melting processes can be found.

4.2 Polarimetric retrieval

The relationship of polarimetric variables and microphysical variables can guide us obtain the “simulated” polarimetric variables from the model mixing ratio (q) and total number concentration (n_t). The relationship evidences the native of polarimetric variables to the DSD which is associated with q and n_t. Hence, one can find the “retrieved” q and n_t or other parameters of DSD from the polarimetric observation with the connection. Polarimetric retrieval which converts polarimetric measurements into DSD parameters is another approach to quantitatively validate model performance. Similar to polarimetric operator, algorithms of polarimetric retrieval are based on several assumptions of hydrometeor characteristics. The uncertainty of assumptions plays significant role in the case of ice-phased particles (ice, snow, and graupel). The inherent complexity of hydrometeor above the melting layer make the retrieval difficult. In order to mitigate the bias from mistake assumptions, various retrieval methods with different assumptions are applied above melting level in this study.

One of the retrieval methods used in the study is established on the look-up tables of the polarimetric operator. As a consequence, derivation of the DSD parameters is based on the same assumptions with the polarimetric operator used in the study. Since it is hard to separate the polarimetric variables of different species in observation, validations are only conducted in stratiform area. The identification of convective and stratiform area follows the method developed by Steiner et al (1995) (Appendix A.2). In stratiform region, polarimetric variables above melting layer can be all regarded as the contribution from snow. By excluding the convective area with strong updraft, the graupel can be eliminated to reduce retrieval uncertainty. Besides, the contribution of ice and cloud species are negligible because of their insignificant size. Therefore, snow is the dominated species above melting layer and "retrieval" variables such as q and n_t of snow can be retrieved from the observed polarimetric variables.

In the polarimetric retrieval method based on look-up tables operator, the contours of Z_{HH} and K_{DP} measurements are found in the snow tables and then the DSD parameters of their intersection are calculated into the "retrieval" model variables. Other retrieval methods also applied in the study include the algorithms developed in Ryzhkov and Zrnic (2019) and Bukovcic et al. (2020) to palliate the uncertainty in the assumption of snow characteristics. Also, for altitude lower than the melting level, retrieval of rain species follows the method mentioned in Lu (2018) (Appendix A.3).

Different from the study in Yu (2018) which only apply polarimetric operator for validation, polarimetric operator and retrievals are both used in this study. In the warm-rain cases, the behaviors of hydrometer particles are relatively simple. Thus, the information of hydrometer characteristics is quite easy to be judge from polarimetric variables directly. For example, higher Z_{DR} value indicates larger rain-drops size. Also more liquid water content always accompanies greater K_{DP} value. Nonetheless, all the judgements mention before fail in the cold-rain cases. Due to the complex characteristics of ice-phased particles, it is hard to get the microphysical conditions from polarimetric measurements with such straightforward relationships. The cold-rain microphysics of Morrison scheme is focused in this study. Thus, it necessitates the polarimetric retrieval which can derive the DSD information quantitatively from their complex relationships above the melting level.

Chapter 5: Results

5.1 Validation with SPOL radar

5.1.1 The validated region and time of the MCS in simulation

It is common for model to generate incorrect location and arriving time of weather system. Therefore, it is important to decide an appropriate analyzing domain and time period for simulation to have a fair comparison between observation and simulation. Since the area sampled by the RHI scan distribute around the northeast of SPOL radar, a fan-shaped domain that cover the scanned area for comparison is determined for the simulation (Fig. 5.1). Simulated data within the domain will be validated with the RHI measurements. Besides the analyzing domain, due to incorrect arriving time, it is necessary to select a suitable time period for comparison.

The analyzed MCS was observed by SPOL radar in the RHI scan mode from 0736 to 0913 UTC. According to the sounding of Pingtung station, the 0-6 km wind shear decline first and then raise from 0300 to 1200 UTC (Fig. 5.3). The decrease and increase of 0-6 km wind shear may result from the approaching and landing MCS (squall line) from southeast China. The period that SPOL radar sampled in RHI mode (0736 to 0913 UTC) happens when the wind shear raises and the magnitude of the wind shear range from 8 to 10 m/s. In the simulation, the timing that squall line arrived in Taiwan straits are several hours late. However, the mean 0-6 km wind shear in the analysis domain of simulation demonstrates similar behavior with the sounding of Pingtung during the squall line arriving period (Fig. 5.4). In the study, simulation of 1330 to 1400 UTC are selected and considered as the same period when the RHI data available (0736 to 0913 UTC). The magnitude of 0-6 km wind shear in 1330 to 1400 UTC of simulation ranges from 8 to 11 m/s which is close to the values of sounding (8 to 10 m/s). Also, both simulation of 1330 to 1400 UTC and observation of 0736 to 0913 UTC have the same increasing tendency of wind shear. Finally, in the maximum Z_{HH} distribution, simulation in 1330 UTC (Fig. 5.5) shows an inverse V-shaped pattern which is similar to the one measured from SPOL radar in 0800 UTC (Fig. 5.6).

In the following sections, polarimetric variables measured by SPOL radar on 14 June is compared with the simulated polarimetric variables from model output. Validation of simulation is conducted in the specified region and time period. The model capability in DSD simulation is examined by the retrieval of SPOL measurements. In order to retain the accuracy of the retrieval methods, only stratiform area of the MCS is analyzed. Also, different retrieval methods with different assumptions are applied to provide a more objective perspective.

5.1.2 Validation in polarimetric variables

Polarimetric variables including Z_{HH}, Z_{DR}, and K_{DP} measured from SPOL radar are averaged and analyzed in contour frequency altitude diagram (CFAD) from 0736 to 0913 UTC (Fig. 5.7 to Fig. 5.12). The peak of Z_{HH} at around 4.5 km can be found in all analyzing times. This signature of Z_{HH} is due to melting of snow causing more liquid water fraction in the ice-phased particles and hence strengthen the Z_{HH} signal that the radar received. Since particles start to melt only after they fall below the 0-degree isotherm, it is reasonable that the melting level is a little bit higher than the height of the Z_{HH} peak. Actually, the melting layer height derived from the Pingtung sounding is about 4.5 to 5 km height (Fig. 5.4) which is higher than or equal to 4.5 km. From 0736 to 0913 UTC, the magnitude of the Z_{HH} peak enhanced over time, especially in the early period (0736 to 0828 UTC). The enhancement of the melting signatures happens simultaneously when the Z_{HH} above the melting layer also increase. Greater Z_{HH} above indicated more or larger ice-phased particles fall to melt which may be the reason that led to the stronger Z_{HH} peak around melting level. Also, Z_{HH} below 0-degree isotherm increase during the early period happens because more raindrops or bigger particles fall from above. Besides the intensification of Z_{HH}, an increasing tendency can also be found in K_{DP}, especially in the upper level (7 to 10 km) and Z_{DR} in the lower level (1 to 3 km) in the beginning of the period (Fig. 5.9 and Fig. 5.11 to Fig. 5.12). All of these phenomena indicate that the MCS is in the developing stage.

Simulated Z_{HH}, Z_{DR}, and K_{DP} which generated through the polarimetric operator have some similarities with the SPOL measurements (Fig. 5.13 to Fig. 5.15). The melting signatures simulated are found around 4.5 km as the same with the observation. Moreover, the magnitude of Z_{HH} peak and the Z_{HH} above and below melting level are enhanced from 1330 to 1400 UTC. Z_{DR} and K_{DP} simulated also demonstrate similar behaviors found in SPOL measurements. In brief, the MCS simulated from 1330 to 1400 UTC strengthens over time which is consistent with the observation. Even though the simulation catches some phenomena observed, several deficiencies can be found. Figure 5.16 demonstrates the comparison of mean Z_{HH}, Z_{DR}, and K_{DP} for all time available from simulation (blue line) and SPOL measurements (gray line). It is pronounced that the simulated Z_{HH} is higher the Z_{HH} measurements. Furthermore, the slope that Z_{HH} decrease with increasing height is much steeper in simulation than the observation. In the examination of simulated K_{DP}, the variation and magnitude of simulated K_{DP} is less than the measured K_{DP} above 5km. Finally, the simulation overestimates the values of Z_{DR} below 4 km and cannot reproduce the increasing Z_{DR} tendency with height. Value of Z_{DR} above the melting layer are almost only dependent on particle density and particle shape which are always constant in simulation (Ryzhkov and Zrnic 2019) (Fig 5.14 and Fig. 5.16). Therefore, it is easy to understand why the simulated Z_{DR} is constant above 0-degree isotherm and hence different from the observation.

5.1.3 Validation in DSD variables

Under exponential distribution assumption, DSD can be represented by two associated parameters such as n_0 and λ or n_t and q (as mentioned in Chapter 3). Mass weighted diameter (D_m) is also one of the parameters that can also characterize DSD. Besides, D_m features the diameter size in the DSD. In the study, q and D_m are used to quantify the magnitude and variation of DSDs. D_m is not simulated in model directly and thus need be derived from the simulated q and n_t:

$$D_m = \frac{4}{\lambda} = 4 \times \left(\frac{q \times \rho_{air}}{\pi \rho_x n_t}\right)^{\frac{1}{3}} \qquad (5.1)$$

In the formula, ρ_x represents particles density which equal to $100 \ \mathrm{kg}/m^3$ for snow and $1000 \ \mathrm{kg}/m^3$ for rain. From the simple formula, one can get the model D_m from the simulated q and n_t. In order to validate the DSD simulated by Morrison scheme, the "true" DSD that composited by reference true q and D_m are need. Therefore, several retrieval methods are applied in the following content to derive the "retrieved" q and D_m from the SPOL measurements.

Snow mixing ratio (above 5 km height) and rain mixing ratio (below 5 km height) are retrieved from the SPOL observations from 0736 to 0913 UTC (Fig. 5.17 to Fig. 5.19). Values of snow mixing ratio varies for different retrieval methods with different assumptions. However, all of them enhance from 0736 to 0913 UTC. The increasing snow mixing ratio is likely the reason that led to the Z_{HH} strengthen mentioned before (Fig. 5.7 and Fig. 5.8). Furthermore, increasing snow mass above melting layer indicates the developing of the MCS again. Regarding the retrieval of rain, the sudden peaks of rain mixing ratio in lower level (1 to 2 km) from 0850 to 0858 UTC corresponds to the increase signature of K_{DP} in the same time and same altitude (Fig. 5.12 and Fig. 5.19). This is due to the highly positive linear relation between K_{DP} and the liquid water content. In contrast to the increasing snow mixing ratio, magnitudes of snow mass weighted diameter (D_m) are nearly the same from 0736 to 0913 UTC (Fig. 5.20 to Fig. 5.22). Except some extreme values found in 0736 and 0742 UTC (Fig. 5.20), there is no significant change of the snow D_m retrieved from 0736 to 0913 UTC. The noisy snow D_m retrievals may result from the nearly-zero K_{DP} in 0736 and 0742 UTC (Fig. 5.11). When the value of K_{DP} approximates to zero, the retrieval algorithm is relatively vulnerable to the measurement error. And the biased K_{DP} induces uncertainty in q and D_m retrieval.

The simulated snow (rain) mixing ratio above (below) 5 km height from 1330 to 1400 UTC are demonstrated in Figure 5.23. It is evident that the snow mixing ratio grow over time. Meanwhile, the values of simulated snow mass weighted diameter (D_m) are nearly unchanged from 1330 to 1400 UTC (Fig. 5.24). These features are similar with the behaviors of retrieved snow q and D_m from the SPOL observations. Actually, from both simulation and retrieval of observations, one can conclude that the MCS strengthen above 5 km over time because the snow mixing ratio increase while the diameter of particles remains the same. The mixing ratio of graupel (white dashed line in Figure 5.23) is negligible compared with the snow mixing ratio. This justifies the assumption in the study that snow species play more significant role than graupel above melting layer height in the stratiform area. Although the tendencies of snow q and D_m are similar between simulation and retrievals, the magnitudes of them are diversed. It is obvious that the model overestimates the snow D_m (Fig. 5.25). In fact, the bias on snow D_m led to the overestimation of simulated Z_{HH} even though the model underestimates the snow q. High value of Z_{HH} always accompanies larger particles sizes and greater number of particles. In the simulation, although the number concentration ($\propto q/D_m$) simulated is less than the retrieval, the exaggerated diameter of snow forces the simulated Z_{HH} higher than the observed Z_{HH}. The rain simulation may subject to the discrepancy of snow DSD simulated above melting layer. In fact, similar overestimation and underestimation also can be noticed in the simulated rain D_m and q. The retrieval of rain D_m (gray lines) is higher than the simulation (blue lines) close to 4 km height (Fig. 5.25) may result from the present of melting snow which contaminate the retrieval of rain species. The values of simulated Z_{DR} are much higher than the SPOL measured Z_{DR} below 5 km (Fig. 5.16) which also imply overestimation of rain D_m, for Z_{DR} is always positively related to the rain drop sizes. Rain drops come from the completely melting snow; therefore, exaggerated size of snow in simulation probably led to the oversized rain particles.

5.2 Simulated microphysical processes analysis

The validated period (1330 to 1400 UTC for simulation and 0736 to 0913 UTC for SPOL observation) only include small portion of the MCS simulation in the analyzed domain. And in the period, simulation overestimates snow D_m and underestimates snow mixing ratio compared to retrievals from observation. A longer inspection that includes the period before validated period may provide more complete understanding of the snow simulation. In Figure 5.26, snow mixing ratio (q) (shaded color) as well as mass weighted diameter (D_m) (white solid line) from 1030 to 1400 UTC on 14 June are demonstrated to include the earlier development of the entire system (longer period and without limited in the stratiform area) in the analyzing domain (same as validated domain). The snow q gradually becomes noticeable after

1230 UTC. This indicates the MCS begins moving in or developing in the analyzed domain at around 1230 UTC. However, the simulated D_m of snow shows few variations except the growth from around 1320 to 1340 UTC above 7 km height (Fig. 5.26). Weather system always associated with different microphysical processes; thus, particles growth or deplete with time. Therefore, it is unrealistic that simulated snow sizes remain almost the same from 1030 to 1400 UTC. In model, simulated snow mixing ratio and total number concentration were determined by advection, sedimentation, diffusion, and microphysical processes. The snow D_m is then derived from the mixing ratio and total number concentration simulated. In the following section, the role of different cold-rain microphysical processes in snow mixing ratio and D_m which is dependent on both q and n_t are analyzed.

5.2.1 CTRL run

In DM microphysical scheme, each microphysical process is a source or sink of mixing ratio (q), total number concentration (n_t) or both of them.

$$\frac{\partial q}{\partial t} = -\nabla \cdot (\boldsymbol{v}q) + \frac{\partial}{\partial z}\left(V_q\right) + \nabla_D q + \left(\frac{\partial q}{\partial t}\right)_{xxx} \qquad (5.2)$$

$$\frac{\partial n_t}{\partial t} = -\nabla \cdot (\boldsymbol{v}n_t) + \frac{\partial}{\partial z}\left(V_{n_t}\right) + \nabla_D n_t + \left(\frac{\partial n_t}{\partial t}\right)_{xxx} \qquad (5.3)$$

The first three terms on the right-hand side of the prognostic equations of q and n_t are advection, sedimentation, and turbulent diffusion. The last terms in two equations represent microphysical processes. $\left(\frac{\partial q}{\partial t}\right)_{xxx}$ and $\left(\frac{\partial n_t}{\partial t}\right)_{xxx}$ are the microphysics rate of q (kg/kg sec^{-1}) and n_t (m^{-3} sec^{-1}). "xxx" represents particular microphysical process such as aggregation or deposition which can vary the values of q and n_t over time. The cold-rain microphysical processes of snow are detailed in Appendix (A.4).The increment or decrement of q and n_t (Δq and Δn_t) in each time step equal to the product of microphysics rate and the time step (Δt, in sec).

$$\Delta q = \left(\frac{\partial q}{\partial t}\right)_{xxx} \times \Delta t \qquad (5.4)$$

$$\Delta n_t = \left(\frac{\partial n_t}{\partial t}\right)_{xxx} \times \Delta t \qquad (5.5)$$

Compared to the original q and n_t, integration over each time step generates new q, n_t and also the new D_m which can be derived from the new q and n_t. In order to understand the roles of different cold-rain microphysical processes in snow q and snow D_m, the increments or decrements of them are decomposed into contributions from different microphysical processes (Fig. 5.27 and Fig. 5.28). Also, a longer period (1030 to 1330 UTC) before the validation is analyzed to understand the ins and outs that cause the validated results.

In Figure 5.27, significant increase in the variations of snow mixing ratio from these microphysical processes don't appear until 1230 UTC. It consists with time that snow mixing ratio start to increase (Fig. 5.26). That is, the MCS begins to intensify in the analyzed domain after 1230 UTC in the simulation. The three dominated microphysical processes that increase the snow mixing ratio are deposition (green dashed line), snow accretion with rain and cloud (pink dashed and solid lines). These processes enhance snow q due to stronger updrafts associated with system development and more vapor, cloud, and rain in to the upper levels. Deposition which shifts the vapor into snow is triggered by increasing of water vapor. Also, more rain and cloud increase the opportunity that snow collects them and hence increase the size and mass of itself in the accretion terms. The increment of snow D_m turns pronounced at around 1200 UTC (Fig. 5.28). Accretion terms of rain and cloud are not only significant in snow mixing ratio increment but also play important roles in snow D_m. Another noticeable process in variation of snow D_m is the autoconversion of cloud, snow to graupel (red solid line). Similarly, the enhancement of this graupel autoconversion process resulted from more cloud transported upward. This autoconversion term increase the snow D_m by removing smaller snow; hence the remaining large snow led to the larger diameter derived. However, autoconversion of cloud, snow to graupel can sometimes decrease the snow D_m if the diameter of removed snow is greater than the current D_m. Actually, the diameter of removed snow is around 0.6 mm according to the formula used in Morrison scheme (Ikawa et al. 1991). The detail derivation of the formula is described in Appendix (A.5).

5.2.2 Sensitivity experiments

In attempt to understand the reason of Morrison scheme overestimating the snow D_m while underestimating the snow mixing ratio; also, to examine the response of Morrison two moment scheme after modifications associated with the microphysical processes, sensitivity experiments are designed and applied in this study. Figure 5.29 demonstrates the distribution of snow D_m and n_t from SPOL retrieval and model simulation above 5 km height during the validation period (0736 to 0913 UTC or SPOL retrievals and 1330 to 1400 UTC for simulation). With the exponential distribution assumption of DSD, the snow water content only relies on the D_m and n_t. Snow water content equals snow mixing ratio multiplied by dry air density. The tilted yellow lines are the contour of snow water content and hence were determined from the coordinated values of D_m (x-axis) and n_t (y-axis). Figure 5.29 indicates that the Morrison scheme tends to generate oversized snow particles and lower number concentration compared with the SPOL retrievals in the validated period (1330 to 1400 UTC). Actually, we can find that the simulated D_m of snow is nearly unchanged before and during the validated period (1030 to 1400 UTC), even when the snow mixing ratio is nearly zero (1100 to 1230 UTC) in Figure 5.26. Overall, the snow D_m of SPOL retrievals distribute from 0.2 to 1.27 mm and most of their D_m value are equal or less than 0.6 mm. In contrast, most of the snow D_m in simulation are greater than 0.8 mm (Fig. 5.29). This means that the autoconversion (snow, cloud to graupel) process mentioned before tends to increase snow D_m in the simulation (D_m>0.6 mm, detailed in Appendix A.5) while decrease or unchanged the snow D_m of SPOL retrieval ($D_m \leq$0.6mm). It is easy to imagine that if model generated oversized and fewer snow particles previously, the autoconversion term will intensify the overestimation of snow D_m in the later time steps.

In order to avoid the vicious circle, total number concentrations of snow are multiplied by 100 and 1000 while retain the magnitude of snow mixing ratios to lower the snow D_m in two sensitivity experiments: NS100 and NS1000. The sensitivity experiments restart from 1200 to 1400 UTC and the modifications of snow n_t are only applied in 1200 UTC, that is, the beginning of the integration of the sensitive tests. In the upper left picture of Figure 5.30, we can find that the D_m of NS100 (blue contour) and NS1000 (red contour) distributed almost less than 0.6 mm compared with the CTRL run (black contour) at 1200 UTC because of the n_t modification.

Besides the sensitivity experiments that revise the snow n_t to control the influence of the autoconversion term, additional three experiments are designed to reduce the microphysics rates of the autoconversion process directly. In fact, the coefficient for the collection efficiency of snow for cloud (eci) affects the riming degree of snow particles and hence influence the process that riming snow converts into graupel. According to the formula used in Morrison two moment scheme, the microphysics rate of the autoconversion process is proportional to the square of eci (Appendix A.3). Kajikawa (1974) derived the eci dependency on the snow and cloud particles size in laboratory. The corresponding eci value of the simulated snow and cloud D_m according to the function from Kajikawa (1974) is smaller than 0.1. However, the default constant of eci in Morrison two moment scheme is 0.7. Therefore, three additional sensitivity experiments that alter eci from 0.7 into 0.5, 0.3, and 0.1 (ECI05, ECI03, and ECI01) are restarted from 1200 to 1400 UTC. The three sensitivity experiments associated with eci revision are expected to lower the magnitude of snow D_m by lessen the microphysics rates of the autoconversion of graupel from snow and cloud. All tests run in the study are arranged in table 5.1.

In NS100 and NS1000, the reduced snow D_m in 1200 UTC return into the larger size quickly once the integration start (Fig. 5.30). The results indicate that the initially separated distributions of CTRL (black contour), NS100 (blue contour), and NS1000 (red contour) gradually coincide together from 1200 to 1300 UTC. The recovery of NS100 and NS1000 also accompany the increasing snow mixing ratio compared with CTRL; however, their distributions are exactly the same at 1300 UTC. The increment of snow mixing ratio and D_m from different microphysical processes at 1201 UTC are showed in figure 5.31. Compared to the CTRL (upper left and right), NS100 (middle left and right) and NS1000 (bottom left and right) generate stronger increment of snow mixing ratio and snow D_m. Although the snow D_m increment of graupel autoconversion (red solid line) indeed decrease, the increment in both snow mixing ratio and D_m of deposition (green dashed line) greatly increase compared with the CTRL. The deposition (process of vapor to snow) is probably the reason which pushed NS100 and NS1000 back to the greater snow D_m simulated despite the approximated-zero increment from the autoconversion of graupel. Consequently, NS100 and NS1000 generated similar results with the CTRL one at 1300 UTC.

For the ECI05, ECI03, and ECI01 experiments, on the other hand, perform better than the CTRL run. However, the smaller snow D_m that we desired in the simulation is insignificant compared with the CTRL (left of Fig. 5.32). No matter if eci is set to 0.5, 0.3, or 0.1, the snow D_m are indeed smaller than the snow D_m in CTRL. Besides, ECI05, ECI03, and ECI01 simulate slightly higher snow mixing ratio than the CTRL one (texts in right of Fig. 5.32). The increment of oversized snow D_m of ECI experiments (left of Fig. 5.33) are suppressed compared with the CTRL run (bottom left of Fig. 5.28), and the increments of suppressed snow D_m were indeed resulted from the smaller graupel autoconversion term (red solid line). Comparing the smaller eci values experiments compared with the default one, the results indicate that not only depressed the snow D_m, but also increase the cloud D_m (Fig. 5.34). In Morrison two moment scheme, cloud is the only SM species; therefore, the D_m of cloud can almost reflect the magnitude of cloud mixing ratio simulated whereas the total number concentration of cloud is constant. Smaller eci led to less cloud droplets collected by snows and hence more cloud mixing ratio retained and finally greater cloud D_m found. The phenomenon is most pronounced in ECI01 which has the smallest eci value.

In brief, two types of sensitivity experiment (NSxxx and ECIxx) are designed to improve the DSD simulation of Morrison scheme; however, fail to suppressed simulated snow D_m. Although the ECIxx experiments indeed decrease the snow D_m and increase the snow mixing ratio, the improvements are limited. All these imply that the underlying cause of bias in Morrison scheme has not been found.

Chapter 6: Conclusion and discussion

6.1 Conclusion

In this research, the simulation with Morrison two moment scheme is validated with the polarimetric measurements from SPOL radar. Polarimetric variables have been proven to be related with the storm microphysical processes; therefore, polarimetric variables can examine the performance of microphysics scheme from numerical model. According to Xu and Zipser (2015), vigorous cold-rain microphysical processes as well as strong updraft inherent in the MCS on 14 June; hence, the case was chosen in the study. The MCS was simulated using WRF model with the Morrison scheme which is double moment (DM) in rain, ice, snow, and graupel. Compared to SM scheme, DM scheme simulated both mixing ratio and total number concentration rather than just mixing ratio. Mixing ratio and total number concentration are integration of mass and number on the whole DSD. Hence, DSD in DM scheme can vary with different mixing ratio or total number concentration. On the other hand, DSD in SM scheme is only dependent on mixing ratio. Also, diameter size in DM scheme, unlike the diameter size in SM scheme, is derived with the two prognostic variables under exponential assumption and was expected to be more realistic. In brief, DM has potential to perform better on the DSD simulation which is one of the important characteristics in microphysics. In the study, simulated results were converted into the simulated polarimetric variables to compare with the observations. Besides, DSD parameters including q and D_m were retrieved from SPOL measurements to examined the simulated DSD in Morrison scheme. In order to minimize the retrieval uncertainty, validation is only conducted in the stratiform area which is distinguished from the convective area with the method developed in Steiner et. al. (1995).

The enhancement of simulated Z_{HH} and K_{DP} during the validated period indicates the strengthen of MCS which is also found in the SPOL measurements. Moreover, simulation and observations have similar tendencies of the increasing Z_{HH}, Z_{DR}, and K_{DP}. Although the model catches some phenomena observed, several deficiencies still can be found. Overestimation of Z_{HH} and Z_{DR} in lower levels are found and both the magnitude and variation of K_{DP} underestimate the observations. Also, the variation of Z_{DR} in upper levels cannot be reproduced by Morrison scheme. Actually, the nearly constant Z_{DR} in upper level results from the fact that snow characteristics such as orientation and shape are not considered in Morrison scheme. In the following analysis on DSD parameters, we can conclude that the raising Z_{HH} and K_{DP} in upper level resulted from the increasing snow mixing ratio which can be seen in both simulation and observation. Moreover, despite the underestimation of snow q in Morrison scheme, the exaggerated Z_{HH} value was still generated from the over-simulated snow D_m. Further, the oversized snow particles above are probably the reason that led to the oversized rain drop and overestimation of Z_{DR} below in the simulation.

In the following analysis includes the period before validation, the nearly unchanged snow D_m is inconsistent with the evolution of snow mixing ratio. To understand the role of each cold-rain microphysical processes in snow DSD simulation, increments of snow mixing ratio and D_m contributed from different processes are analyzed. The autoconversion of graupel from cloud-riming snow is one of the dominated processes that result in large increment of snow D_m. Therefore, two kinds of sensitivity experiments designed according to the autoconversion process are run and expected to improve the snow DSD simulation. First, in NS100 and NS1000 experiment, total number concentrations of snow are multiplied by 100 and 1000 to reduce the snow D_m at the initial time of restart run (1200 UTC 14 June). Second, ECI05, ECI03, and

ECI01 alter the default value of collection efficiency of snow for cloud (eci) from 0.7 to 0.5, 0.3, and 0.1. The smaller eci can reduce the degree of snow riming and hence depress the increments of D_m caused by the graupel autoconversion process. The former (NSxxx) modifies the initial condition of snow D_m while the latter (ECIxx) decreases the magnitudes of the microphysics rates directly. Even with the modification of the snow D_m proved to be invalid because the snow D_m and n_t of the sensitivity experiment and CTRL run converge eventually. Although the DSD simulated from ECI05, ECI03, and ECI01 are closer to SPOL retrievals than the CTRL ones, the improvements are limited.

To sum up, Morrison two moment scheme doesn't realize its potential in the snow DSD simulation, especially the snow D_m. The validations on both polarimetric variables and DSD parameters with SPOL observations indicate the overestimation of snow D_m and underestimation of snow mixing ratio. Further, the biased snow simulation above causes negative impact below. The simulated Z_{DR} below melting layer height are found higher than the measured Z_{DR}. Finally, several sensitive tests are applied in attempt to improve the simulation; however, fail to achieve the goal. All these imply that the underlying cause of bias in Morrison scheme has not been found.

6.2 Discussion

There are some results in the research that are worth further discussion. First, the method used to differentiate stratiform and convective area is based on the 2 km Z_{HH} (Steiner et. al. 1995). Hence, the credibility of stratiform area distinguished in simulation may be questioned since the Morrison scheme tends to generate unreasonable Z_{HH}. In fact, this influence in the analysis of the study is limited. The 10 mm/hr rain rate is often used to separate stratiform area ($< 10\mathrm{mm/hr}$) from convective area ($> 10\mathrm{mm/hr}$) which can be the reference to examine the method based on Z_{HH}. In Figure 6.1, most of the data (~90%) classified as stratiform has rain rate less than 10 mm/hr. On the other hand, nearly 50% of convective data has rain rate less than 10 mm/hr. The misclassification of stratiform area is probably due to the overestimation of Z_{HH} in Morrison scheme. Since there is only stratiform area (Chapter 5.1) and all area (Chapter 5.2) analyzed in the study, the high uncertainty exists in convective area won't impact the results much. Another potential problem stems from the fact that validation is conducted in stratiform area while analysis of microphysical processes is in all area. The simulation indeed is different from the simulation without convective area; nevertheless, the difference between them is so small when comparing with the SPOL retrievals in stratiform area (Fig. 5.29). The retrieved snow D_m (n_t) in stratiform area is smaller (larger) than the simulated snow D_m (n_t) even though simulation didn't exclude the convective area.

Although the issue about stratiform identification and analysis mentioned above won't affect the pivotal conclusions, this study may be defective in partiality for cold-rain microphysical processes of snow. Actually, not only microphysical processes but also advection, sedimentation, and diffusion can influence the simulation of snow q and

n_t. In the Chapter 5.2, two kinds of sensitivity tests are performed to suppress the snow D_m simulated; nevertheless, the results leave much to be desired. Maybe the microphysical processes are not the main source or sink of snow properties. Therefore, it is hard to have significant improvement by changing the coefficient of collection efficiency for snow. Also, the complex interaction between species (cloud, rain, ice, snow, and graupel) in Morrison scheme worth more attention. Clearly, a more complete analysis that include different processes (advection, sedimentation, …) may assist the uncover of mechanism of incorrect snow DSD simulation.

References

盧可昕，2018: 利用雙偏極化雷達及雨滴譜儀觀測資料分析 2008 年西南氣流實驗期間強降雨事件的雲物理過程，國立中央大學大氣物理所碩士論文，1-91 頁。

陳勁宏，2018: 不同微物理方案在雲可解析模式的系集預報分析: SoWMEX-IOP8 個案，國立中央大學大氣物理所碩士論文，1-83 頁。

游承融，2019: 利用雙偏極化雷達觀測資料進行極短期天氣預報評估: 2008 年西南氣流實驗 IOP8 期間颮線系統個案，國立中央大學大氣物理所碩士論文，1-92 頁。

Berry, E., and R. Reinhardt, 1974: An analysis of cloud drop growth by collection: Part II. Single initial distributions. *J. Atmos. Sci*., **31**, 1825–1831

Brandes, E. A., G. Zhang, and J. Vivekanandan, 2002. Experiments in rainfall estimation with a polarimetric radar in a subtropical environment. *J. Appl. Meteor.*, **41**, 674–68.

Bukovcic, P., A. Ryzhkov, and D. Zrnic, 2020. Polarimetric Relations for Snow Estimation–Radar Verification. *J. Appl. Meteor.*, **59**, 991–1009.

Ciesielski, P. E., W. M. Chang, S. C. Huang, R. H. Johnson, B. J. D. Jou, W. C. Lee, P. H. Lin, C. H. Liu, and J. Wang, 2010: Quality-Controlled Upper-Air Sounding Dataset for TiMREX/SoWMEX: Development and Corrections. *J. Atmos. Ocean. Technol.*, **27**, 1802-1821

Cohard, J.-M., and J.-P. Pinty, 2000: A comprehensive two-moment warm microphysical bulk scheme. I: Description and tests. *Quart. J. Roy. Meteor. Soc.*, **126**, 1815–1842

Davis, C. A., and W.-C. Lee, 2012. Mesoscale Analysis of Heavy Rainfall Episodes from SoWMEX/TiMREX. *J. Atmos. Sci.*, **69**, 521-537.

Doviak, R., and Zrnic, D. (2006). *Doppler radar and weather observations (2nd ed.)*. Reprint, Mineola, NY: Dover.

Ikawa, M., H. Mizuno, T. Matsuo, M. Murakami, Y. Yamada, and K. Saito, 1991. Numerical Modeling of the Convective Snow Cloud over the Sea of Japan - Precipitation Mechanism and Sensitivity to Ice Crystal Nucleation Rates. *J. Meteorol. Soc.*, **69**, 641-667.

Johnson, M., Y. Jung, D. T. Dawson II, and M. Xue, 2016. Comparison of Simulated Polarimetric Signatures in Idealized Supercell Storms Using Two-Moment Bulk Microphysics Scheme in WRF. *Mon. Wea. Rev.*, **144**, 971-996.

Jung, Y., G. Zhang, and M. Xue, 2008. Assimilation of Simulated Polarimetric Radar Data for a Convective Storm Using the Ensemble Kalman Filter. Part I: Observation Operators for Reflectivity and Polarimetric Variables. *Mon. Wea. Rev.*, **136**, 2228-2245.

Kajikawa, M., 1974. On the Collection Efficiency of Snow Crystals for Cloud Droplets. *J. Meteorol. Soc.*, **52**, 328-336.

Kessler, E., (1969): *On the Distribution and Continuity of Water Substance in Atmosphere Circulations. Meteor. Monogr*., No. 32, Amer. Meteor. Soc., 84 pp.

Mishchenko, M. I., L. D. Travis, and D. W. Mackowski, 1996. T-matrix computation of light scattering by nonspherical particles: a review. *J. Quant. Spectrosc. Radiat. Transfer*, **55(5)**, 535-575.

Morrison, H., J. A. Curry, and V. I. Khvorostyanov, 2005. A New Double-Moment Microphysics Parameterization for Application in Cloud and Climate Models. Part I: Description. *J. Atmos. Sci.*, **62**, 1665-1677.

Morrison, H., and W. W. Grabowski, 2007: Comparison of bulk and bin warm rain microphysics models using a kinematic framework. *J. Atmos. Sci.*, **64**, 2839–2861

Morrison, H., and W. W. Grabowski, 2008. A Novel Approach for Representing Ice Microphysics in Models: Description and Tests Using a Kinematic Framework. *J. Atmos. Sci.*, **65**, 1528-1548.

Morrison, H., G. Thompson, and V. Tatarskii, 2009. Impact of Cloud Microphysics on the Development of Trailing Stratiform Precipitation in a Simulated Squall Line: Comparison of One- and Two-Moment Schemes. *Mon. Wea. Rev.*, **137**, 991-1007.

Ryzhkov, A. V., and D. S. Zrnic (2019). *Radar Polarimetry for Weather Observations.* Switzerland: Springer.

Steiner, M., R. A. Houze Jr., and S. E. Yuter, 1995. Climatological Characterization of Three-Dimensional Storm Structure from Operational Radar and Rain Gauge Data. *J. Appl. Meteor.*, **34**, 1978–2007.

Stensrud, D. J. (2007). *Parameterization Schemes–Keys to Understanding Numerical Weather Prediction Models.* New York: Cambridge University Press.

Straka, J. (2009). *Cloud and Precipitation Microphysics –Principles and Parameterizations.* New York: Cambridge University Press.

Xu, W., E. J. Zipser, Y. L. Chen, C. Liu, Y. C. Liou, W. C. Lee, and B. J. D. Jou, 2012: An Orography-Associated Extreme Rainfall Event during TiMREX: Initiation, Storm Evolution, and Maintenance. *Mon. Wea. Rev.*, **140**, 2555-2574.

Xu, W., and E. J. Zipser, 2015: Convective intensity, vertical precipitation structures, and microphysics of two contrasting convective regimes during the 2008 TiMREX. *J. Geophys. Res. Atmos.*, **120**, 4000–4016.

Ziegler, C. L., 1985: Retrieval of thermal and microphysical variables in observed convective storms. Part I: Model development and preliminary testing. *J. Atmos. Sci.*, **42**, 1487–1509

Appendix

A.1 Introduction of polarimetric variables

Polarimetric measurements indicate different physical meaning and are widely applicable. Five common use polarimetric variables are described here (Z_{HH}, Z_{DR}, K_{DP}, LDR, and ρ_{HV}). Z_{HH} is the radar reflectivity at horizontal polarization in a unit volume (mm^6 m^{-3}). The variable is positive correlated to hydrometeor sizes and number concentration measured. Also, liquid-phased particles have greater Z_{HH} than the ice-phased particles. On the other hand, differential reflectivity (Z_{DR}) computed from the ratio of Z_{HH} and Z_{VV} (reflectivity at vertical polarization).

$$Z_{DR} = 10 \times \log(Z_{HH}/Z_{VV}) \qquad (\mathrm{A.1})$$

Z_{DR} is associated with rain drop size below the melting layer and larger rain size exhibits higher Z_{DR}. However, above the melting layer, the signal of Z_{DR} is smaller and the value of Z_{DR} is nearly determined by the shape and orientation of ice-phased particles (unrelated to the DSD characteristic). Specific differential phase (K_{DP}) is also dependent on hydrometeor sizes and number concentration. Besides, particles shape and orientation influence the value of K_{DP} derived. Since K_{DP} is proportional to the third moment of DSD, it is always used to estimate liquid water content or mixing ratio below the melting layer. Linear depolarization ratios (LDR) and cross-correlation coefficient (ρ_{HV}) are useful in data quality control. Compared to rain and dry snow (-34 ~ -25 dB), melting snow has larger LDR (-15 ~ -20 dB); however, the LDR of them still less than zero. Larger LDR (>0 dB) and smaller ρ_{HV} (< 0.5) are always dominated by noise.

A.2 Identification of stratiform area

Steiner et. al. (1995) developed algorithms that separate the convective system into convective and stratiform regions. The convective and stratiform regions are distinguished on the basis of the intensity and sharpness of the peaks of Z_{HH} intensity at 2 km height. Three criteria for convective area identification are:

- ✓ *Intensity*: For any grid points in the analyzed domain with Z_{HH} equal to or over than 40 dBZ are regard as the convective centers.
- ✓ *Peakedness*: First, average of Z_{HH} are taken over the surrounding background of the grid point. The surrounding area contain grid points within 11 km of radius. Second, derive the difference of Z_{HH} between the center grid point and background regions. If the difference ΔZ_{dif} is greater than the specified values $\Delta \mathrm{Z}$, than the center grid point is determined as a convective center.

$$\Delta Z_{dif} = Z_{cen} - Z_{bg} \qquad (\mathrm{A.2})$$

$$\Delta \mathrm{Z} = \begin{cases} 10, & Z_{bg} < 0 \;\; dBZ \\ 10 - Z_{bg}^2/180, & 0 \le Z_{bg} < 42.43 \;\; dBZ \\ 0, & Z_{bg} \ge 42.43 \;\; dBZ \end{cases} \qquad (\mathrm{A.3})$$

- ✓ *Surrounding area*: For any grid points that are identified as the convective centers, the surrounding area of the points are also considered as the convective regions. The radius of the surrounding area is intensity-dependent.

Finally, the remain regions that don't satisfied any of the above three criteria are identified as stratiform area. In the study, the algorithms are applied in both SPOL measurements and model simulation to filter out the convective area for further analysis.

A.3 Polarimetric retrieval methods

A.3.1 Retrieval method of rain species

Mixing ratio and total number concentration of rain species are retrieved with polarimetric radar measurements below 4.5 km height. And then the DSD parameters D_m of rain is derived that is analyzed with q in the study. The derivation of D_m and q of rain species follows Lu (2018) and Doviak and Zrnic (2006) respectively.

$$rain\ D_m = {Z_{HH}}^{0.042}\left(0.0477{Z_{DR}}^3 - 0.1445{Z_{DR}}^2 + 0.5846Z_{DR} + 0.8240\right) \qquad (A.4)$$

$$rain\ q = \rho_{air} \times 0.34(K_{DP}\lambda)^{0.702} \qquad (A.5)$$

In these equations, the D_m and mixing ratio of rain can be retrieved from the measured Z_{HH}, Z_{DR}, and K_{DP}.

A.3.2 Retrieval method of snow species

The retrievals of snow species are more difficult than the rain species because of the inherent complexity of snow properties. Therefore, in the study more than one retrieval methods and assumptions are applied to give unbiased results. Bukovcic et. al. (2020) and Ryzhkov and Zrnic (2019) provides several methods to derive snow D_m and mixing ratio.

$$snow\ D_m = -0.1 + 2.0\,\eta, \qquad \eta = \left(\frac{Z_{DP}}{K_{DP}\lambda}\right)^{1/2} \quad (A.6)$$

λ here means the wavelength of radar (λ of SPOL radar equal to 10 cm) rather than the slope parameter of DSD. Formula (a) calculates snow D_m from Z_{DP} and K_{DP} measured from SPOL radar. According to Ryzhkov and Zrnic (2019), the result of the retrieval method is sparse from different snow shape and orientation; however, is affected by the degree of riming. Hence, it is appropriate to applied the equation in lower temperature area where the riming seldom happens.

$$snow\ D_m = 1.24\left[F_{shape}F_{orient}\right]^{1/3}\xi,\quad \xi = \left(\frac{Z_{HH}}{K_{DP}\lambda}\right)^{1/3} \quad \text{(A.7)}$$

$$F_{orient} = \frac{1}{2}exp(-2\sigma^2)[1+\exp(-2\sigma^2)] \qquad (\mathrm{A.8})$$

Compared to formula (A.6), formula (A.7) is sensitive to the orientation and shape specified; nevertheless, is rarely influenced the snow DSD, density, and degree of riming. F_{orient} is parameter of orientation, and is determined from the standard deviation of canting angle σ, smaller σ (~10) happens for dendrites or plates, while larger σ (~40) happens for snow aggregates. F_{shape} is parameter of shape and is affected by the axis ratio of snow particles. Value of F_{shape} ranges from 0.4 to 0.1 for axis ratio increases from 0.4 to 0.8 (Ryzhkov and Zrnic 2019).

$$snow\ \ q = \ 4.46\times 10^{-3}\frac{K_{DP}\lambda}{1-{Z_{DR}}^{-1}} \div \rho_{air} \quad (\mathrm{A.9})$$

$$snow\ q = \frac{10.2\times 10^{-3}}{\left(F_{orient}F_{shape}\right)^{0.66}}(K_{DP}\lambda)^{0.66}{Z_{HH}}^{0.28} \div \rho_{air} \quad (\mathrm{A.10})$$

Formula (A.9) and (A.10) derive snow mixing ratio from K_{DP} and Z_{DR} and K_{DP} and Z_{HH} respectively. And compared with (A.10), formula (A.9) is less sensitive to the orientation and shape of snow particles.

Besides the methods mentioned above, the method that developed on the snow tables of dual-polarimetric operator is also applied in the study. As a consequence, derivation of the DSD parameters and mixing ratio is based on the same assumptions with the polarimetric operator. In the polarimetric retrieval method, the contours of Z_{HH} (red solid line and shaded color) and K_{DP} (white solid line) measurements are found in the snow tables and then the DSD parameters (n_0 and λ) of their intersection are calculated into the "retrieval" model variables q, n_t ,and finally D_m.

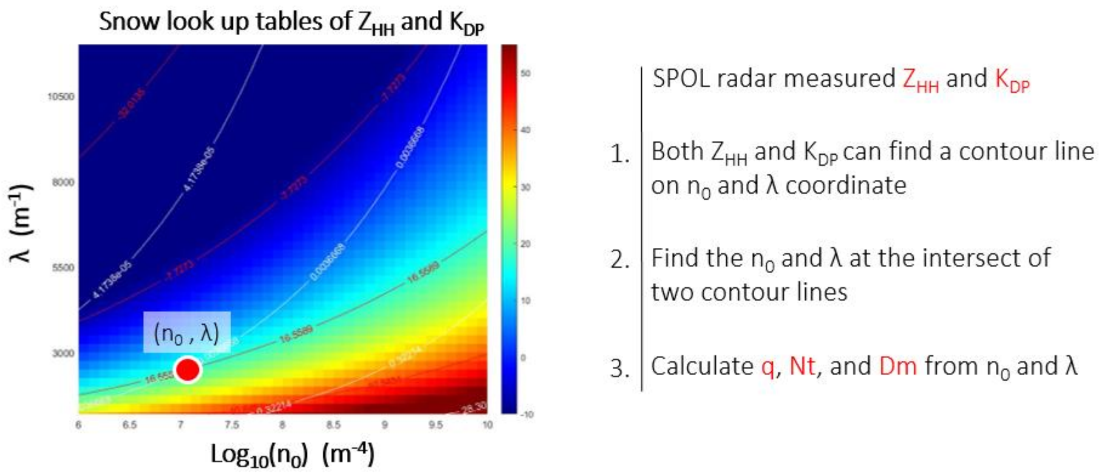

A.4 Cold-rain microphysics of snow in Morrison scheme

The cold-rain microphysical processes of snow are analyzed in this study (Fig. 5.27, Fig. 5.28, Fig. 5.31, and Fig. 5.31). Several microphysical processes with insignificant magnitude (such as ice multiplication from snow) compared with others are not demonstrated and discussed in the analysis. Several processes that influence the snow mixing ratio or number concentration are described below.

Accretion of cloud or rain droplets to snow (c or r to s)

The gradual collection of cloud or rain droplets as snow particles fall through the atmosphere. The process led to increase in snow mixing ratio and growth in snow diameter (D_m). Also, during the process, the mixing ratio of cloud or rain will decrease. The process of accretion of cloud droplets to snow (c to s) is represented by pink solid line in figures. While the process of accretion of rain droplets to snow (r to s) is represented by pink dashed line in figures.

Autoconversion of graupel due to collection of cloud or rain droplets by snow (s, c or r to g)

The cloud or rain droplets collected by snow result in the riming snow. Part of the cloud or rain-riming snows convert into the embryos of graupel. The process causes part of the snow and cloud or rain mixing ratio transferred into the graupel species. Also, the total number concentration of snow and cloud or rain will decrease. The process increase or decrease the D_m of snow depending on the magnitude of snow D_m and the removed D_m which can be derived from the removed mixing ratio and total number concentration of snow (the derivation is described in next section A.5). In the figures (Fig. 5.27, Fig. 5.28, Fig. 5.31, and Fig. 5.31), autoconversion due to cloud collected by snow is plotted in red solid line. While autoconversion due to rain collected by snow is plotted in thin blue dashed line.

Autoconversion of graupel due to collection of snow by rain (r, s to g)

Graupel generation due to collection of snow by rain. The process causes part of the snow and rain mixing ratio transferred into the graupel species. Autoconversion due to snow collected by rain is plotted in thick blue dashed line.

Autoconversion of ice crystal to snow (i to s)

Autoconversion of ice crystal to snow transfers mixing ratio and number concentration of ice species to snow species. The process is represented by thick blue solid line in figures.

Deposition (v to s)

When the mixing ratio of water vapor greater (less) than the ice saturation mixing ratio, deposition (sublimation) happens. Deposition process transfer mixing ratio of vapor to snow while sublimation transfer the mixing ratio of snow to vapor. Deposition process led to the snow D_m growth. Green dashed line is used to represent deposition process in figures.

Collision of ice and rain and add to snow (r, i to s)

The process describes the generation of snow due to the collision of ice and rain particles. The process increase snow mixing ratio and total number concentration and is represented by light blue solid line.

A.5 Autoconversion of graupel from cloud-riming snow

The process belongs to cold-rain microphysical processes and hence works only when the temperature less than $0°\mathrm{C}$ in Morrison scheme. The process will result in increment (or decrement) of snow mixing ratio (q) and total number concentration (n_t) in every time step. The microphysics rates in mixing ratio $PGSACW$ $(kg/kg\ sec^{-1})$ and total number concentration $NSCNG$ $(m^{-3}sec^{-1})$ of the processes are:

$$PGSACW = CONS17 \times dt \times n_{0s} \times {q_c}^2 \times {a_{sn}}^2 \div \left(\rho \times {\lambda_s}^{2b_s+2}\right) \quad (\mathrm{A.11})$$

$$CONS17 = \frac{24\pi \times \rho_{850} \times eci^2 \times \Gamma(2b_s + 2)}{8 \times \left(\rho_g - \rho_s\right)} \quad (\mathrm{A.12})$$

$$NSCNG = \frac{\rho_s}{\rho_g - \rho_s} \times PGSACW \div \left(m_{g0} \div \rho\right) \quad (\mathrm{A.13})$$

dt or Δt is the time step in simulation (sec). n_{0s} is the intercept parameter of snow. q_c is the mixing ratio of cloud species. a_{sn} and b_s (fixed constant) are the parameter associated with fall velocity of snow ($v = a_{sn}D^{b_s}$). λ_s is the slope parameter of snow. ρ, ρ_g, ρ_s is density of air, graupel, and snow respectively. m_{g0} is the mass of initial graupel.

The removed mass and total number concentration of snow correspond to the "removed" mass weighted diameter (D_m).

$$D_{removed} = 4000 \times \left(\frac{\Delta q_s}{\pi \rho_s \Delta n_s}\right)^{\frac{1}{3}} \cong 0.6\, mm \qquad (A.14)$$

$$\frac{\Delta q_s}{\Delta n_s} = \frac{PGSACW \times \Delta t}{NSCNG \times \Delta t} = \frac{4.8 \times 10^{-10}}{\rho} \qquad (A.15)$$

The snow D_m in next time step will increase or decrease is dependent on whether the current snow D_m larger than the removed diameter $D_{removed}$ or not in the process.

Figures

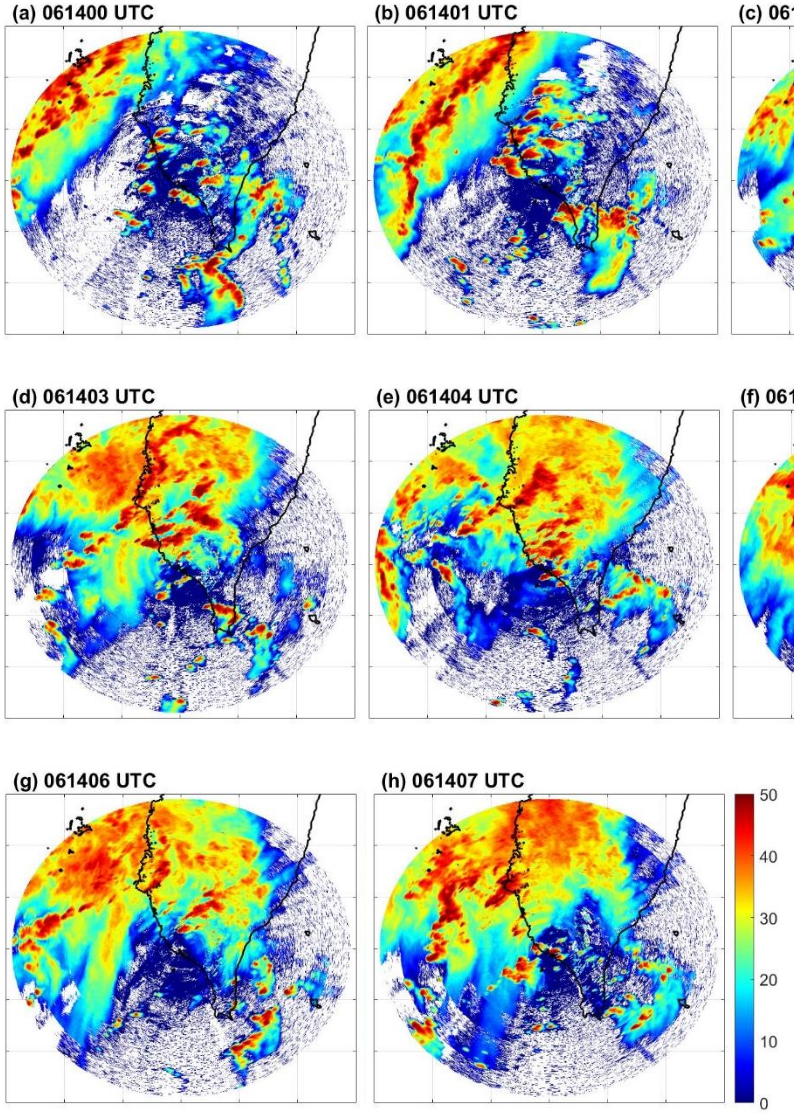

Figure 2.1 The maximum Z_{HH} of the approaching MCS (squall line) on 14 June 2008 which led to precipitation in southwest Taiwan.

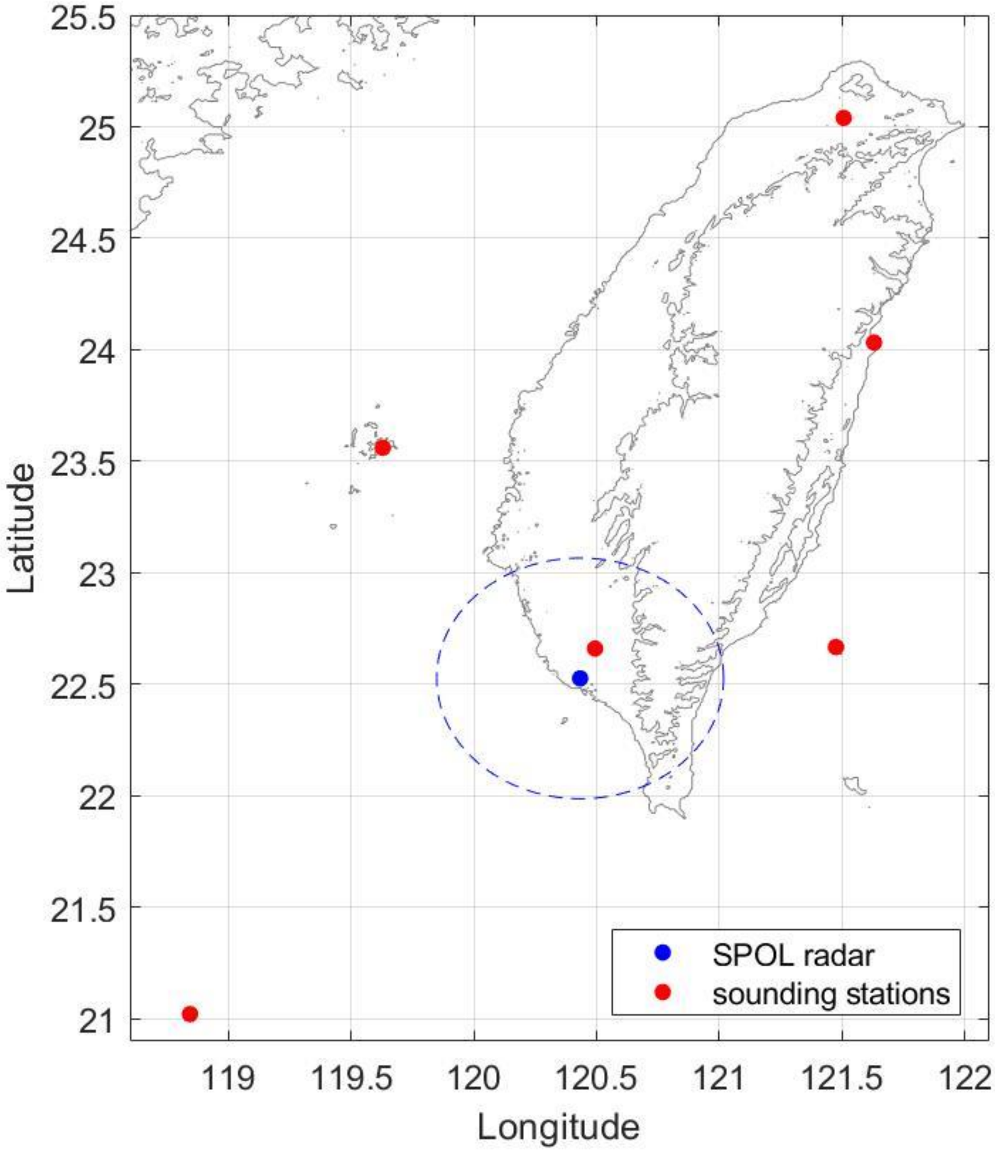

Figure 2.2 Locations of sounding stations and SPOL radar. Pingtung station is located in the northeast of the SPOL radar. The blue dashed line circles the SPOL radar with the range distance equal 60 km.

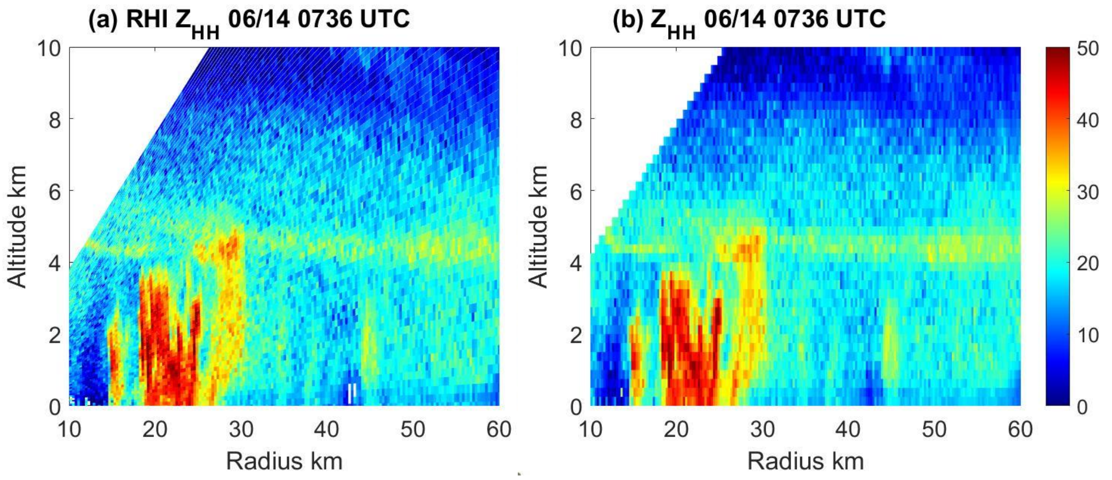

Figure 2.3 Z_{HH} profile at 0736 UTC on 14 June measured from SPOL radar (left) and Z_{HH} profile after interpolation (right).

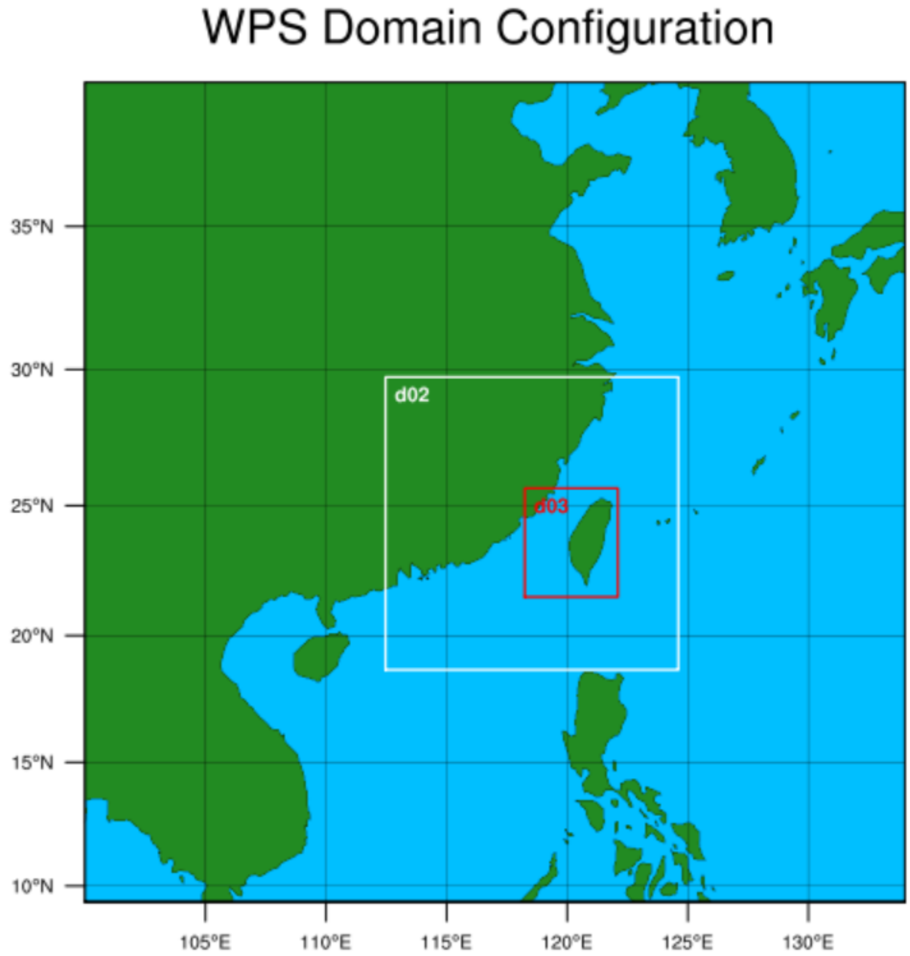

Figure 3.1 Experimental domain setting.

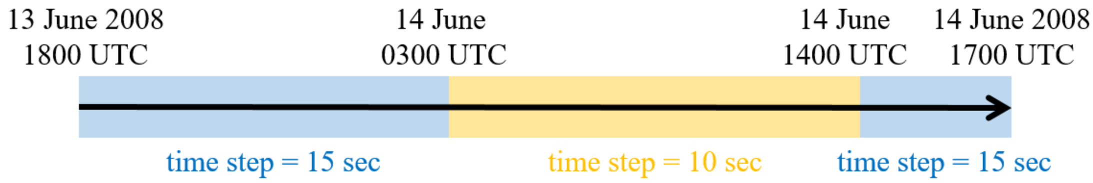

Figure 3.2 Configuration of time in simulation. An initial run and two restart run composite the whole simulation.

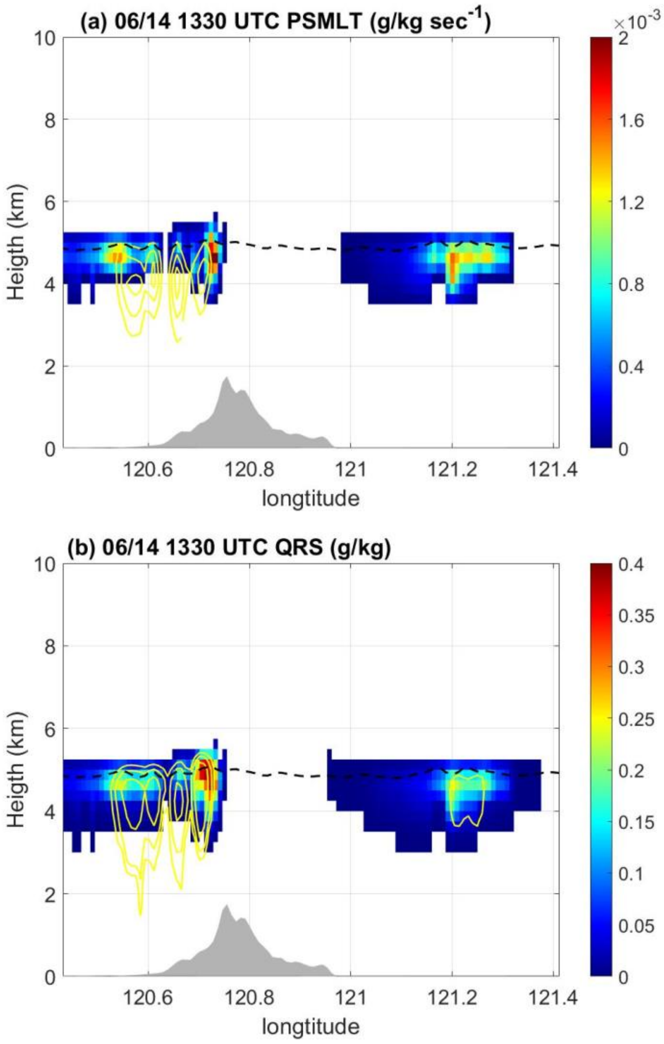

Figure 4.1 The upper panel demonstrates the microphysics rates of melting snow (PSMLT, shaded color) and melting graupel (yellow solid contour: 0.5, 1, 1.5$\times 10^{-3}$ g/kg s^{-1}). The lower picture demonstrates the mixing ratio of melting snow (QRS, shaded color) and melting graupel (yellow solid contour: 0.5, 0.1, and 0.2 g/kg). Black dashed line indicates the melting layer height. Gray shaded area is the terrain area.

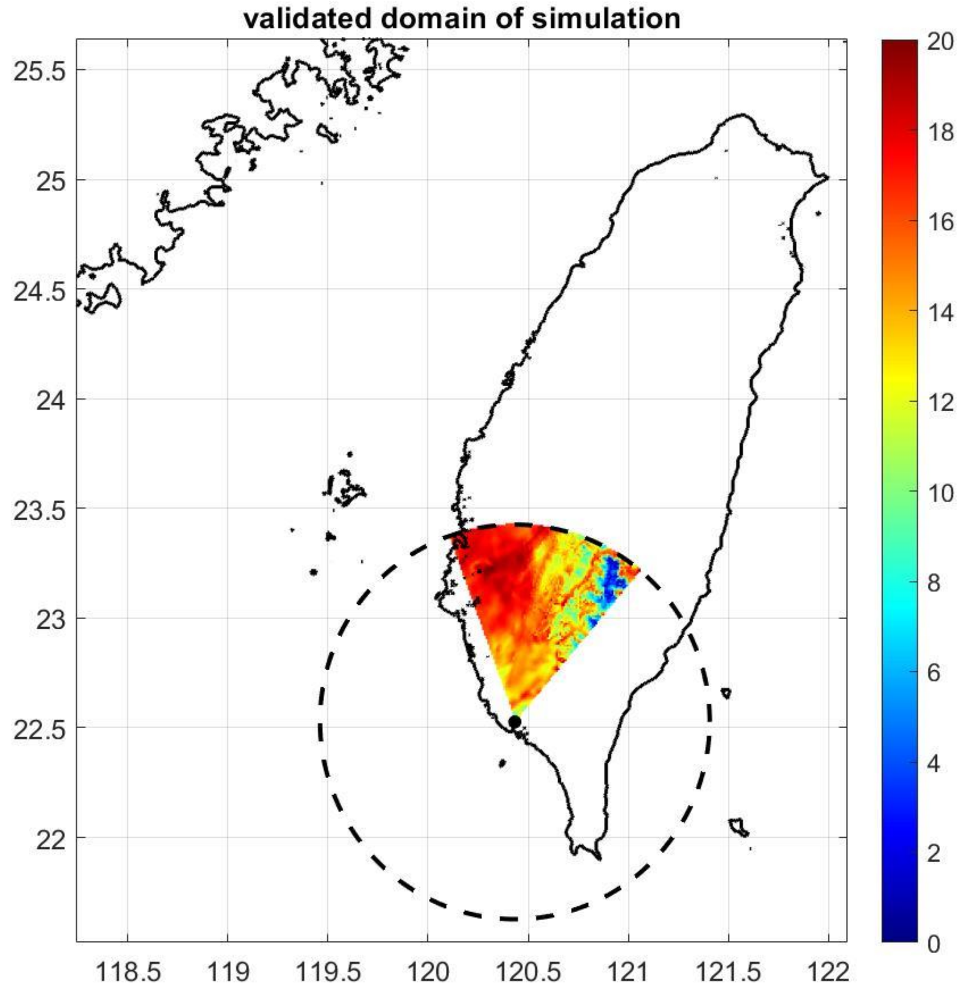

Figure 5.1 The black dashed line circles the area that range distance of SPOL radar less than 100 km. The shaded color indicates the 0-6km wind shear (m/sec) of simulation at 0000 UTC on 14 June. The shaded area is the validated domain of simulation.

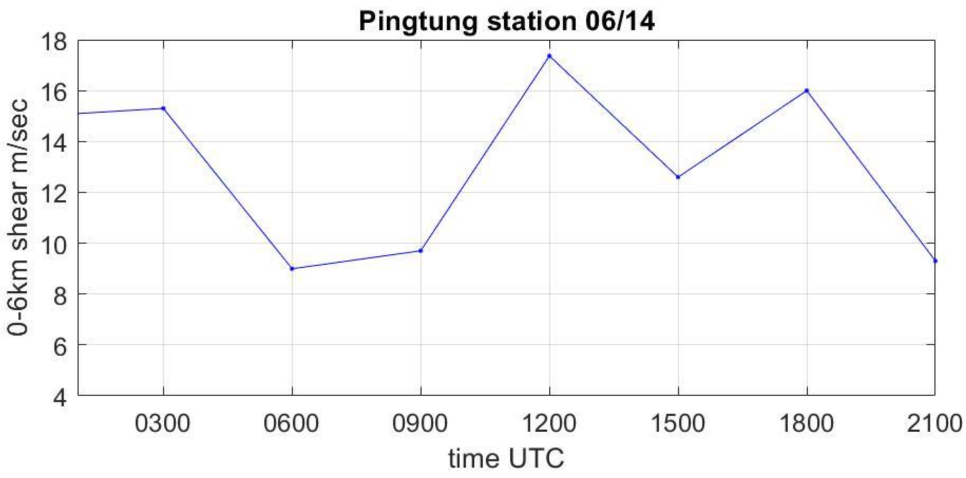

Figure 5.2 0-6 km wind shear at Pingtung station on 14 June.

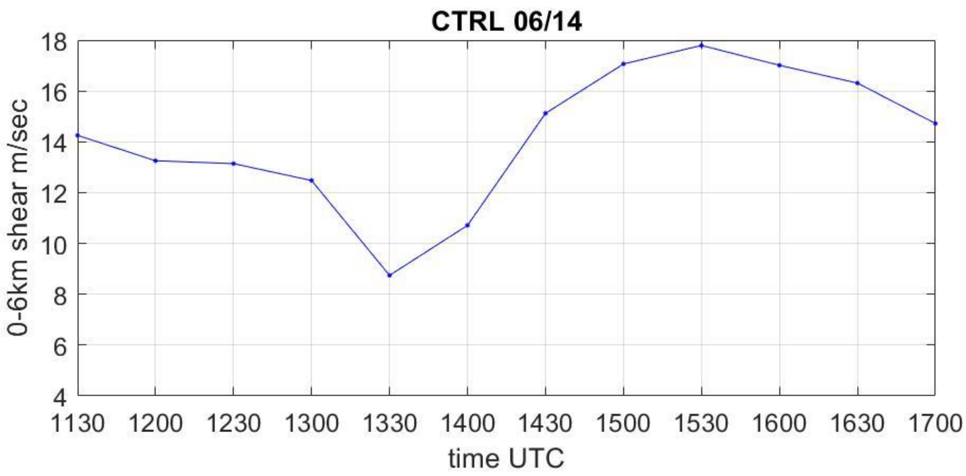

Figure 5.3 Average of 0-6 km wind shear in the validated area (Fig. 5.1) of simulation on 14 June.

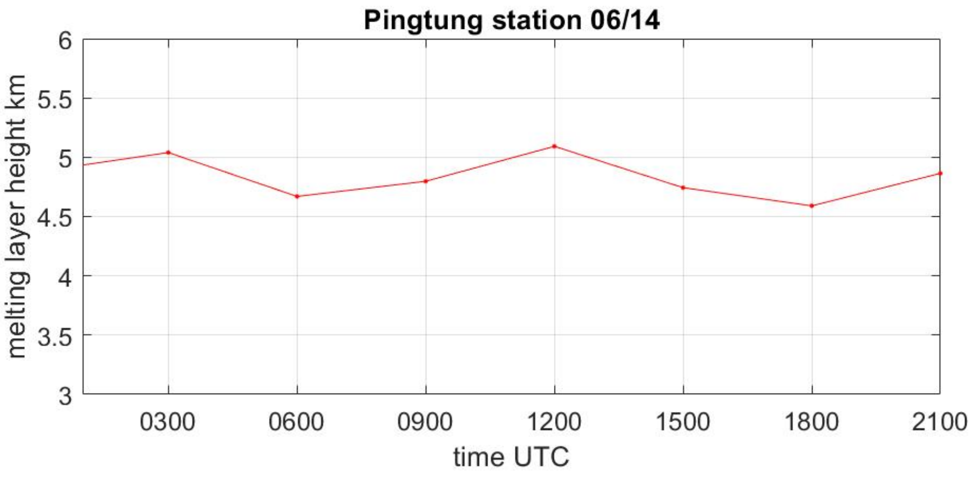

Figure 5.4 Melting layer height at Pingtung station on 14 June.

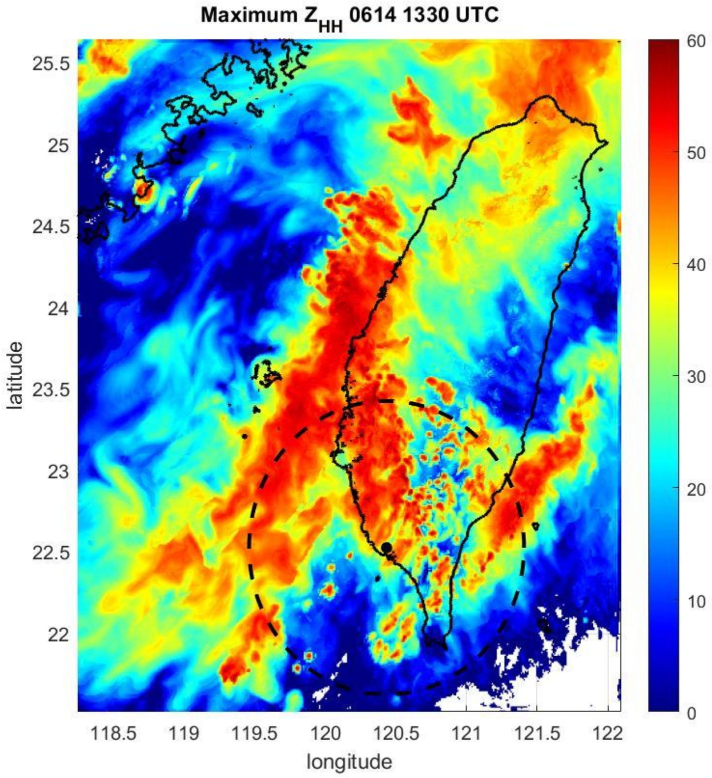

Figure 5.5 Simulated maximum Z_{HH} at 1330 UTC on 14 June. The black point indicates the location of SPOL radar. The black dashed line circles area with range distance less than 100 km.

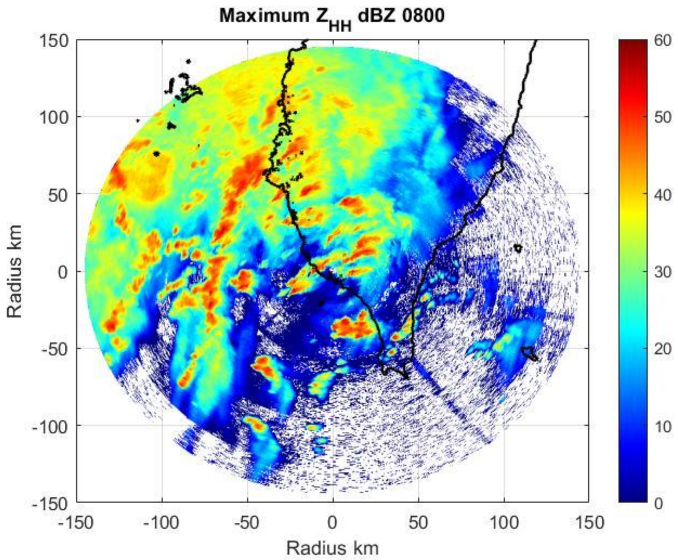

Figure 5.6 Maximum Z_{HH} measured by SPOL radar at 0800 UTC on 14 June. The shaded area is within the 100 km range distance of SPOL radar.

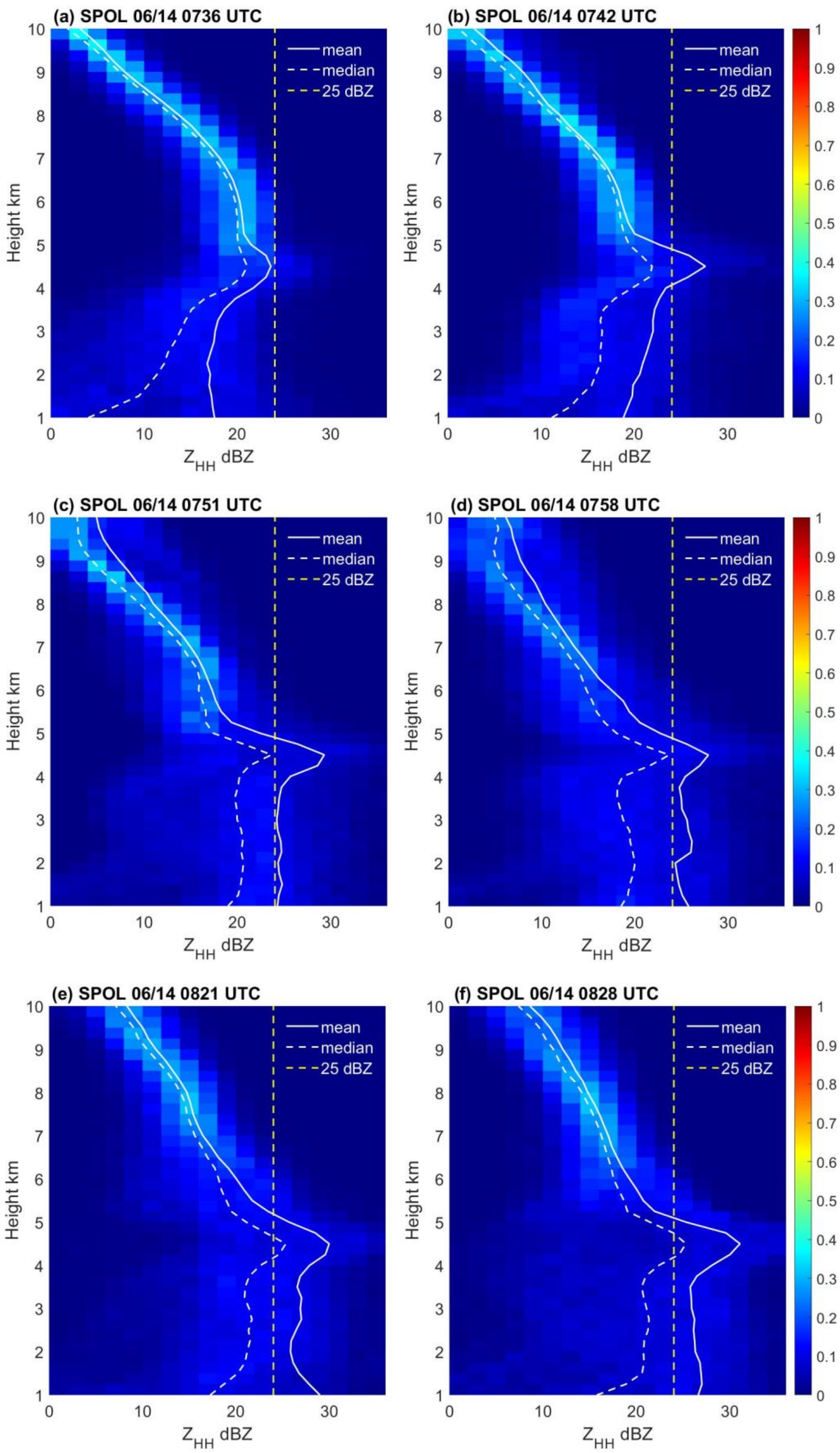

Figure 5.7 Shaded color is CFAD of Z_{HH} measured by SPOL radar from 0736 to 0828 UTC. White solid line is the mean Z_{HH}, and white dashed line is the median Z_{HH}.

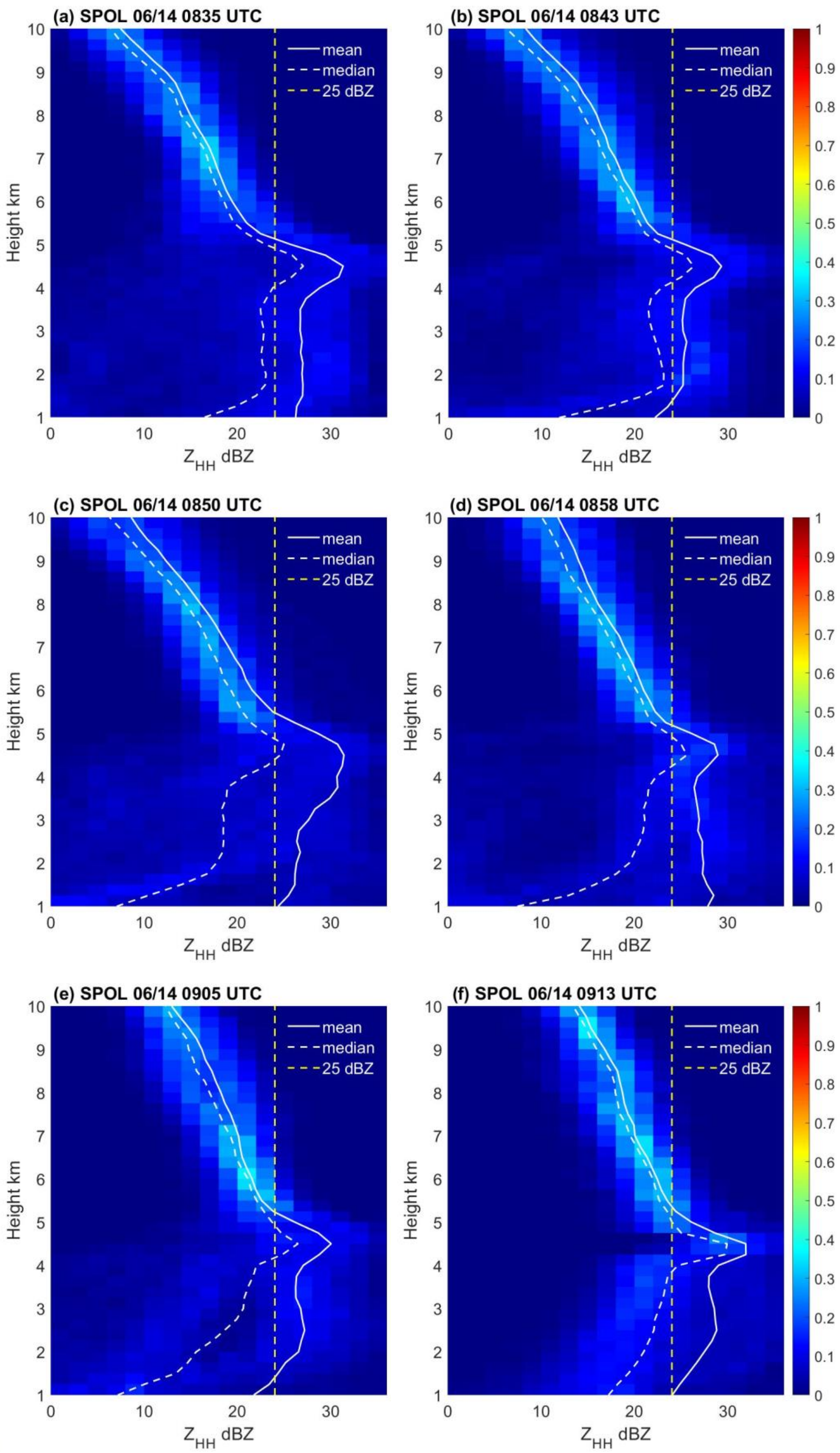

Figure 5.8 Shaded color is CFAD of Z_{HH} measured by SPOL radar from 0835 to 0913 UTC. White solid line is the mean Z_{HH}, and white dashed line is the median Z_{HH}.

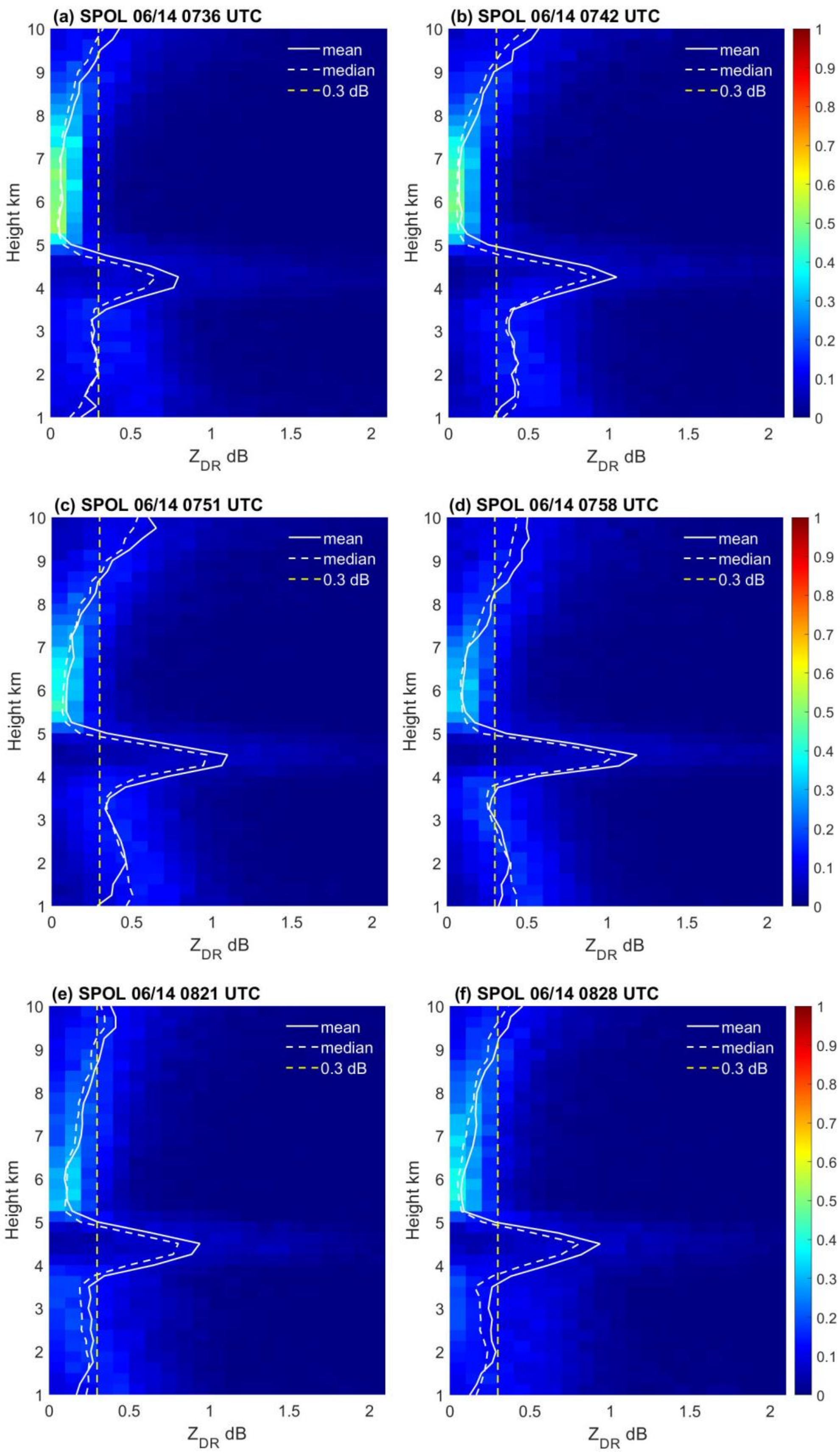

Figure 5.9 Shaded color is CFAD of Z_{DR} measured by SPOL radar from 0736 to 0828 UTC. White solid line is the mean Z_{DR}, and white dashed line is the median Z_{DR}.

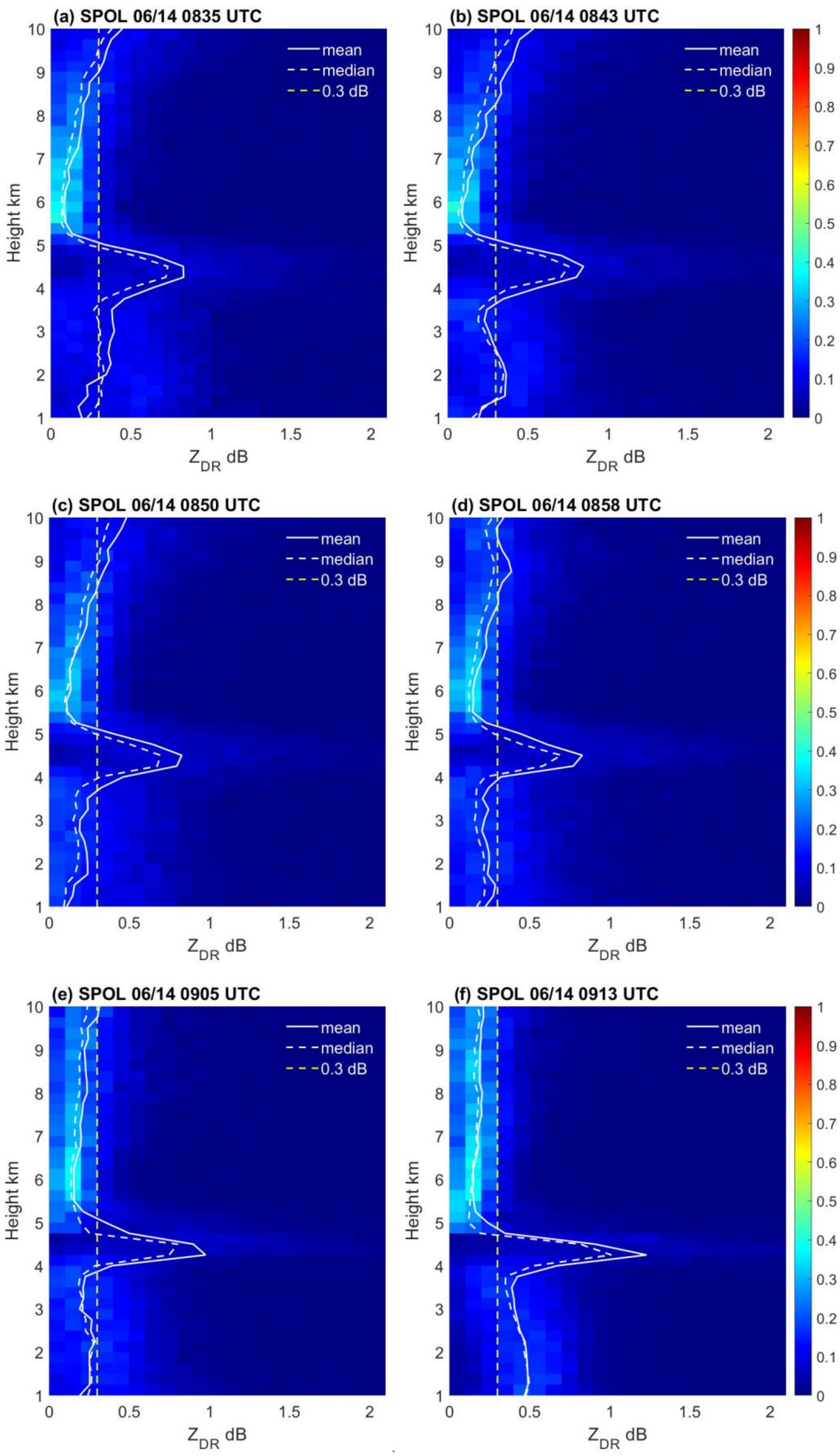

Figure 5.10 Shaded color is CFAD of Z_{DR} measured by SPOL radar from 0835 to 0913 UTC. White solid line is the mean Z_{DR}, and white dashed line is the median Z_{DR}.

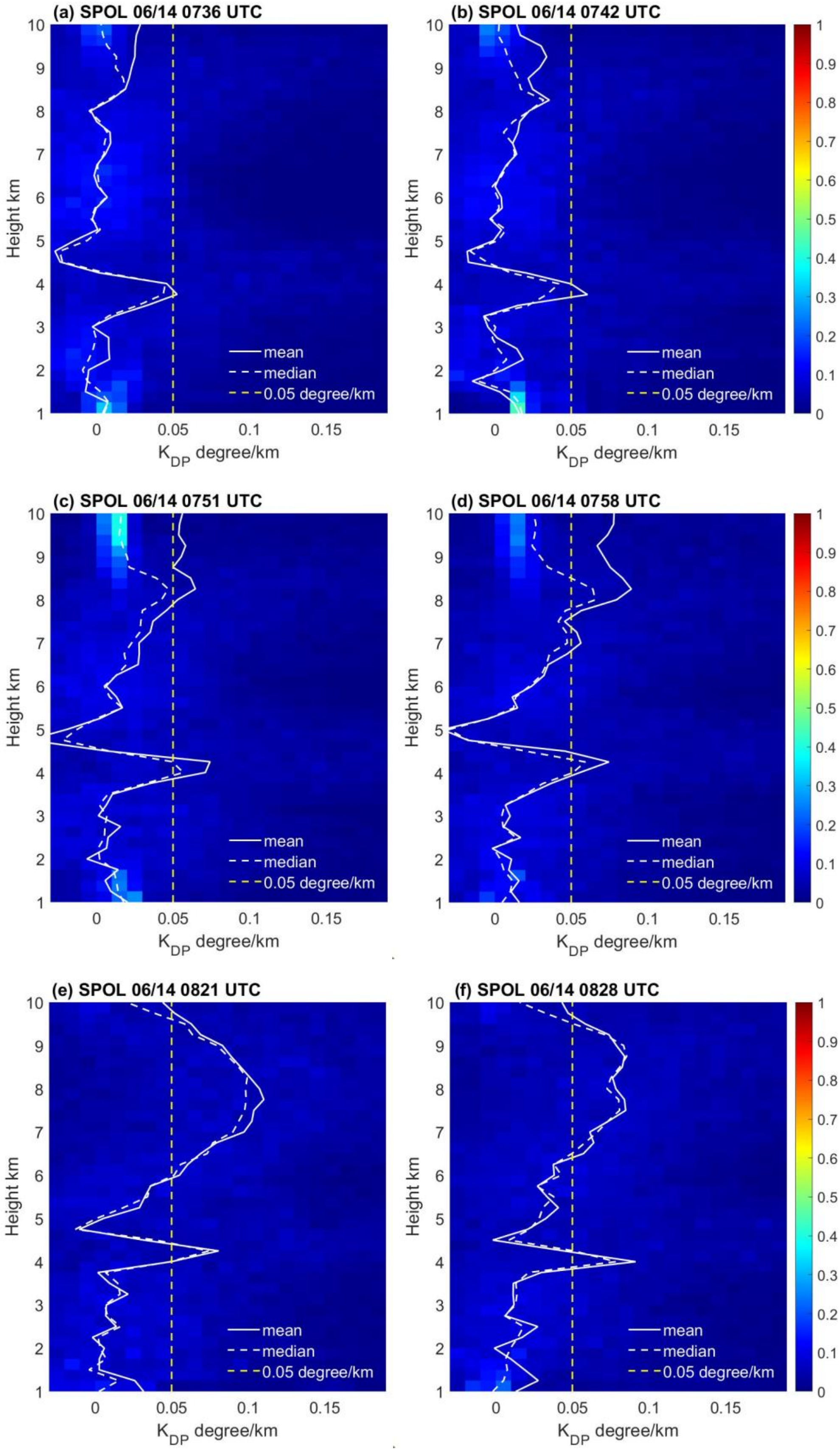

Figure 5.11 Shaded color is CFAD of K_{DP} measured by SPOL radar from 0736 to 0828 UTC. White solid line is the mean K_{DP}, and white dashed line is the median K_{DP}.

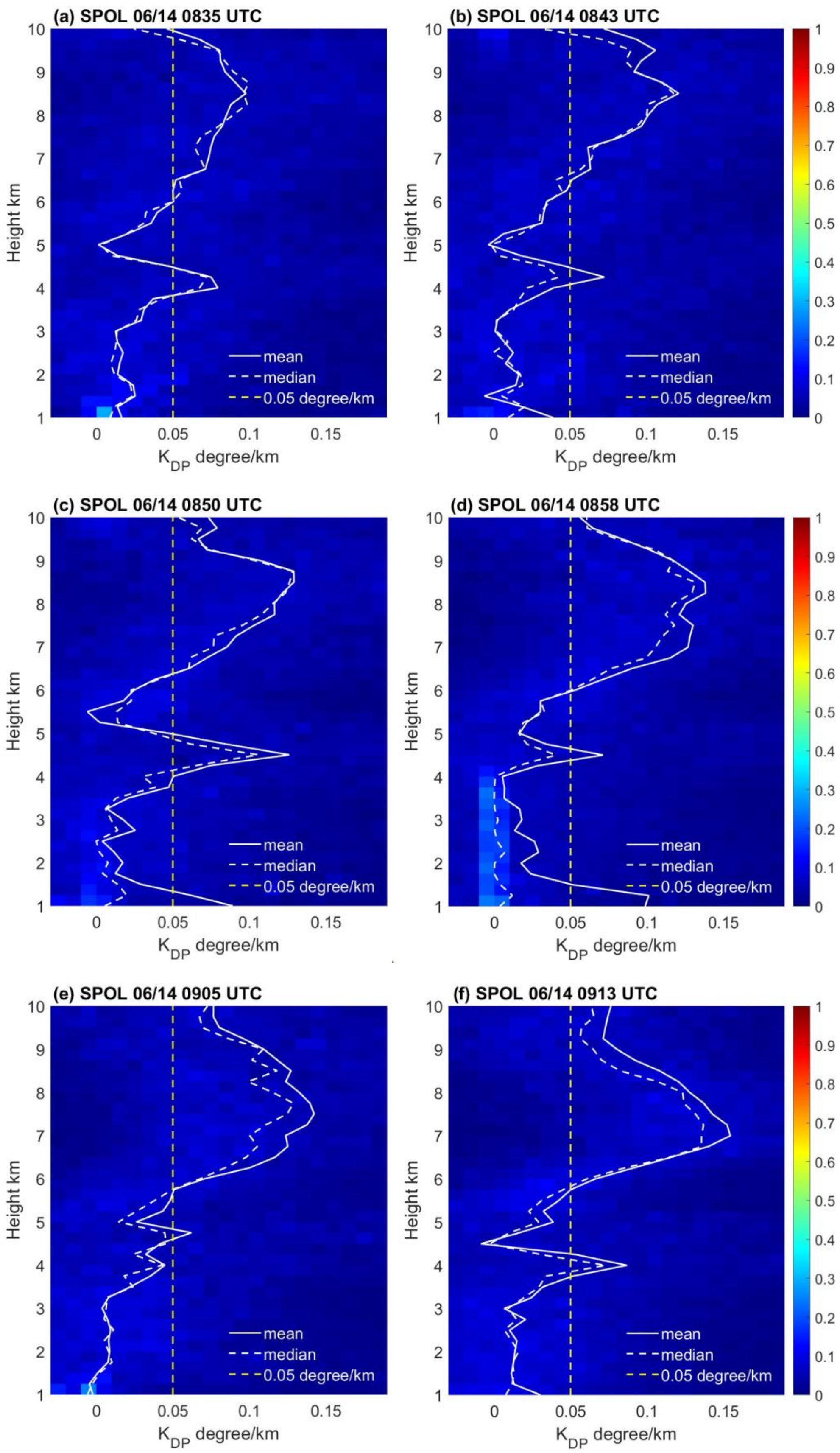

Figure 5.12 Shaded color is CFAD of K_{DP} measured by SPOL radar from 0835 to 0913 UTC. White solid line is the mean K_{DP}, and white dashed line is the median K_{DP}.

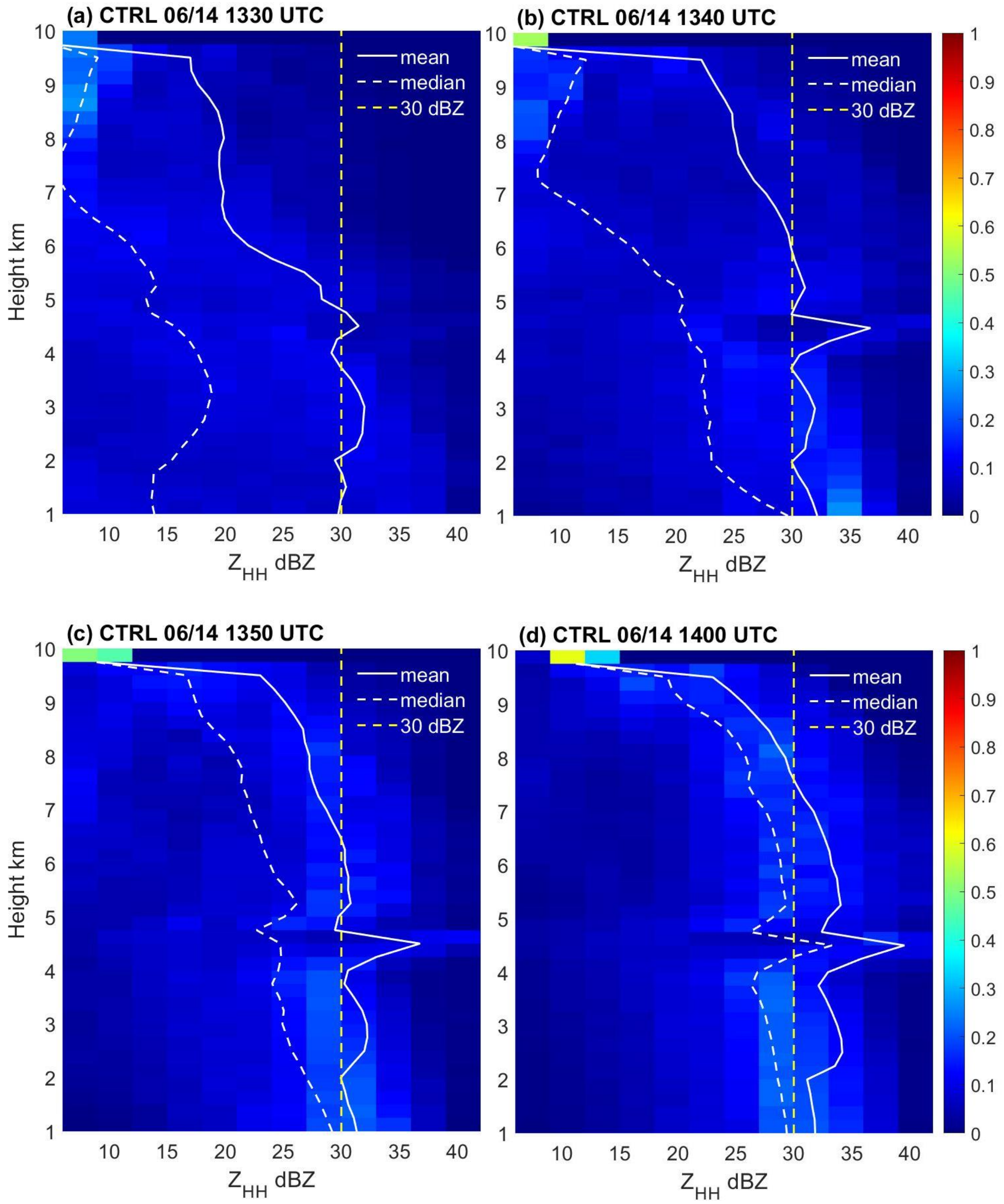

Figure 5.13 Shaded color is CFAD of Z_{HH} simulated from 1330 to 1400 UTC. White solid line is the mean Z_{HH}, and white dashed line is the median Z_{HH}. Yellow dashed lines are the reference line (30 dBZ).

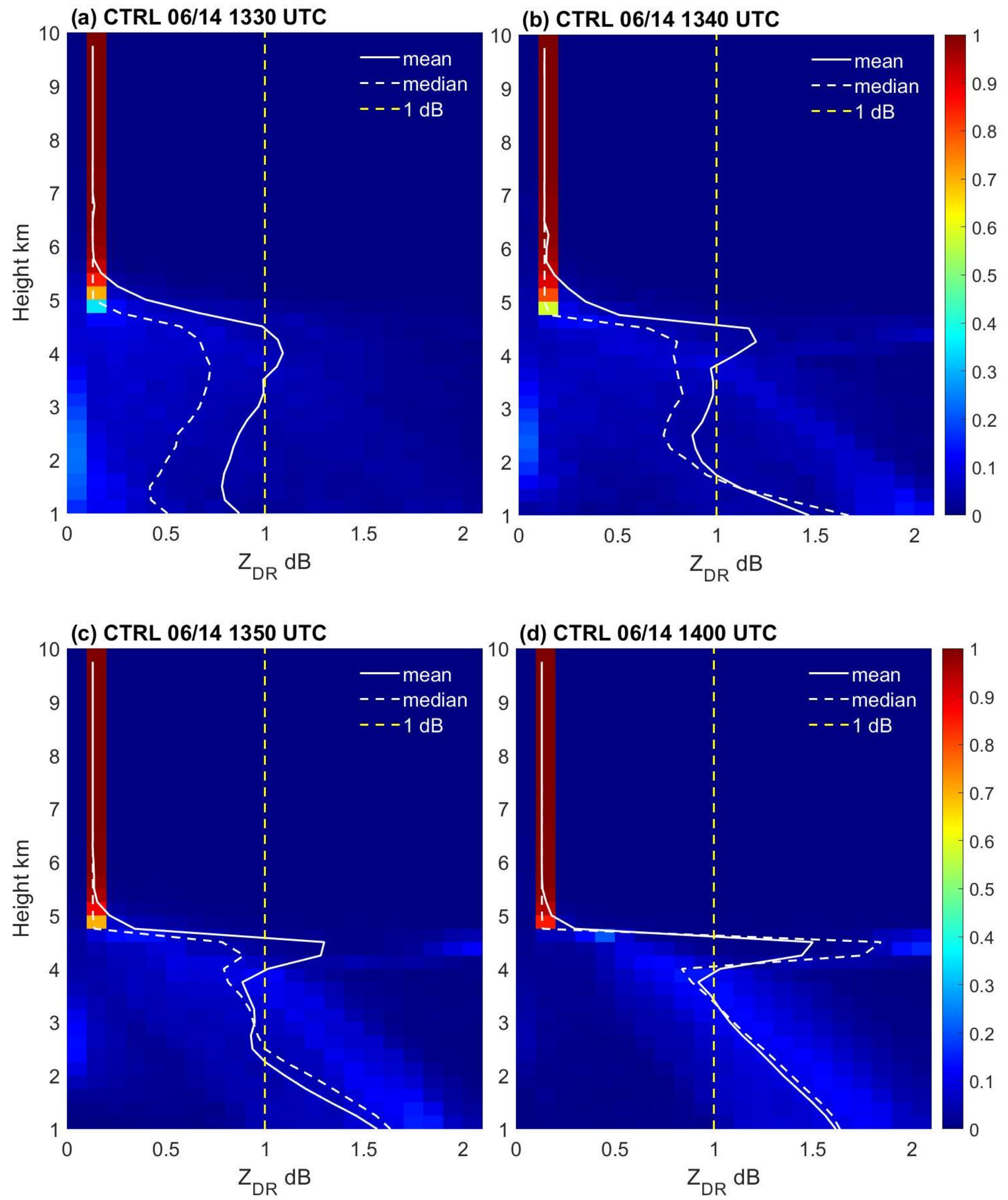

Figure 5.14 Shaded color is CFAD of Z_{DR} simulated from 1330 to 1400 UTC. White solid line is the mean Z_{DR}, and white dashed line is the median Z_{DR}. Yellow dashed lines are the reference line (1 dB).

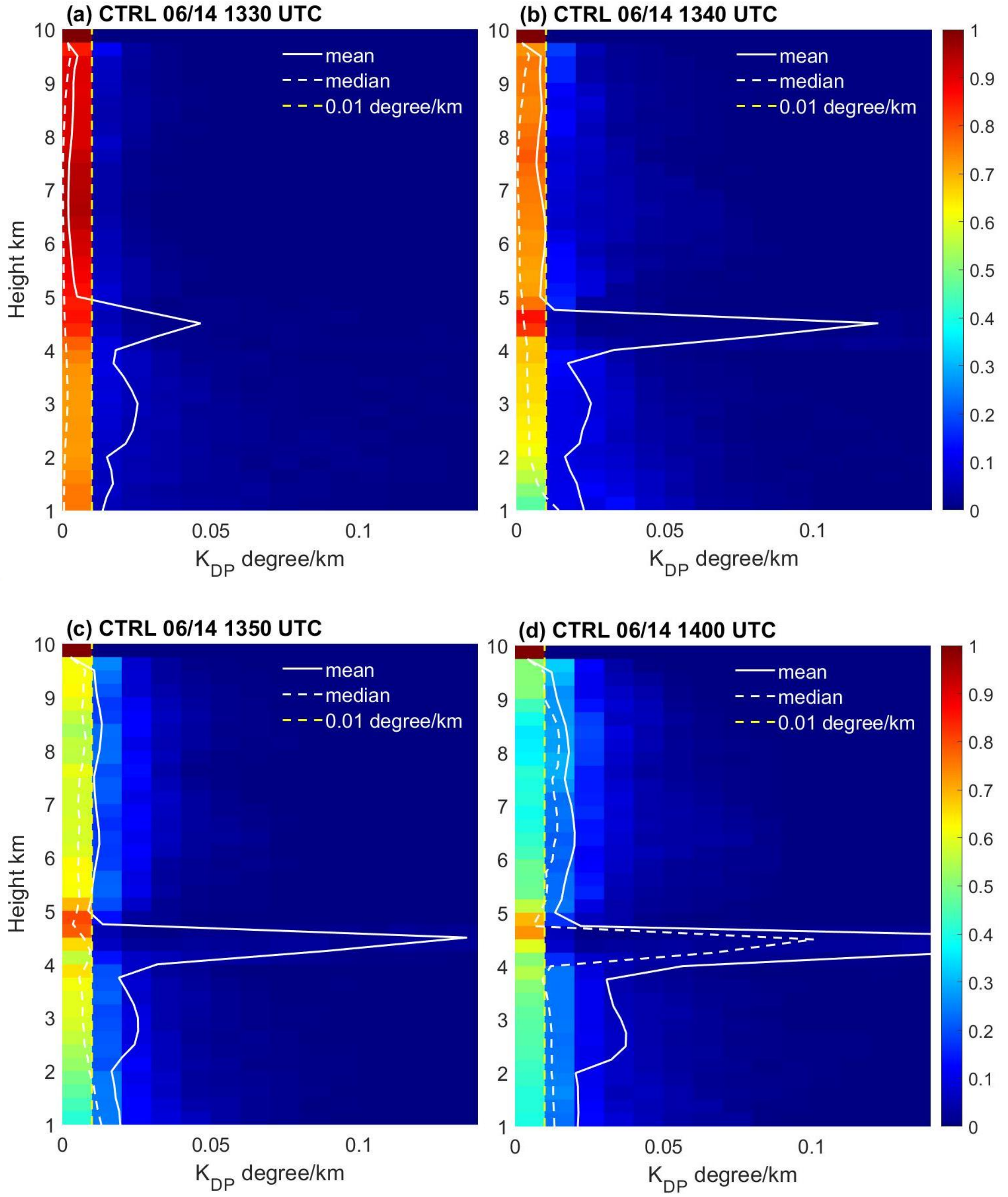

Figure 5.15 Shaded color is CFAD of K_{DP} simulated from 1330 to 1400 UTC. White solid line is the mean K_{DP}, and white dashed line is the median K_{DP}. Yellow dashed lines are the reference line (0.01 degree/km).

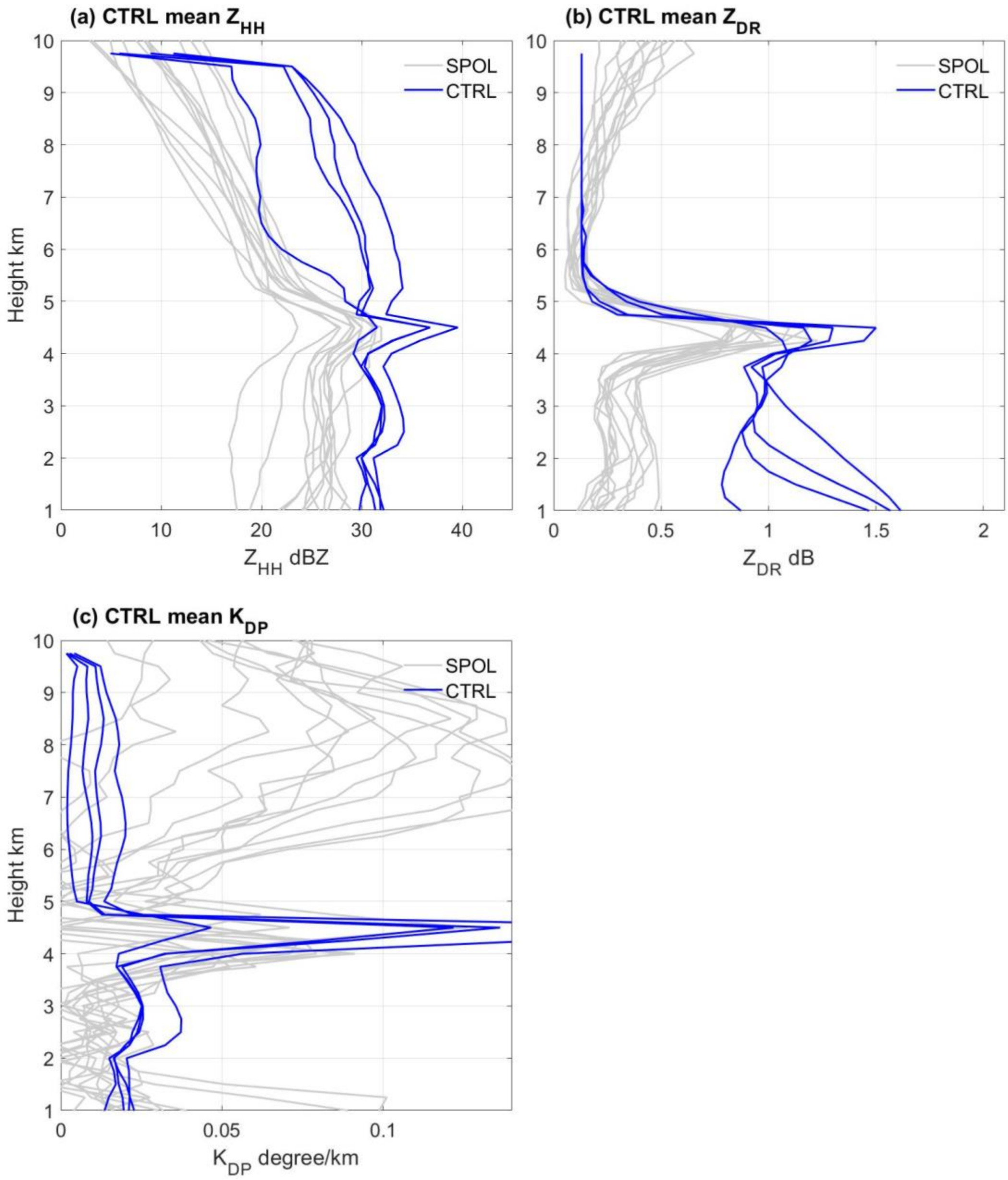

Figure 5.16 Blue solid lines are mean of simulated Z_{HH}, Z_{DR}, and K_{DP} from 1330 to 1400 UTC. Gray solid lines are mean of measured Z_{HH}, Z_{DR}, and K_{DP} from 0736 to 0913 UTC.

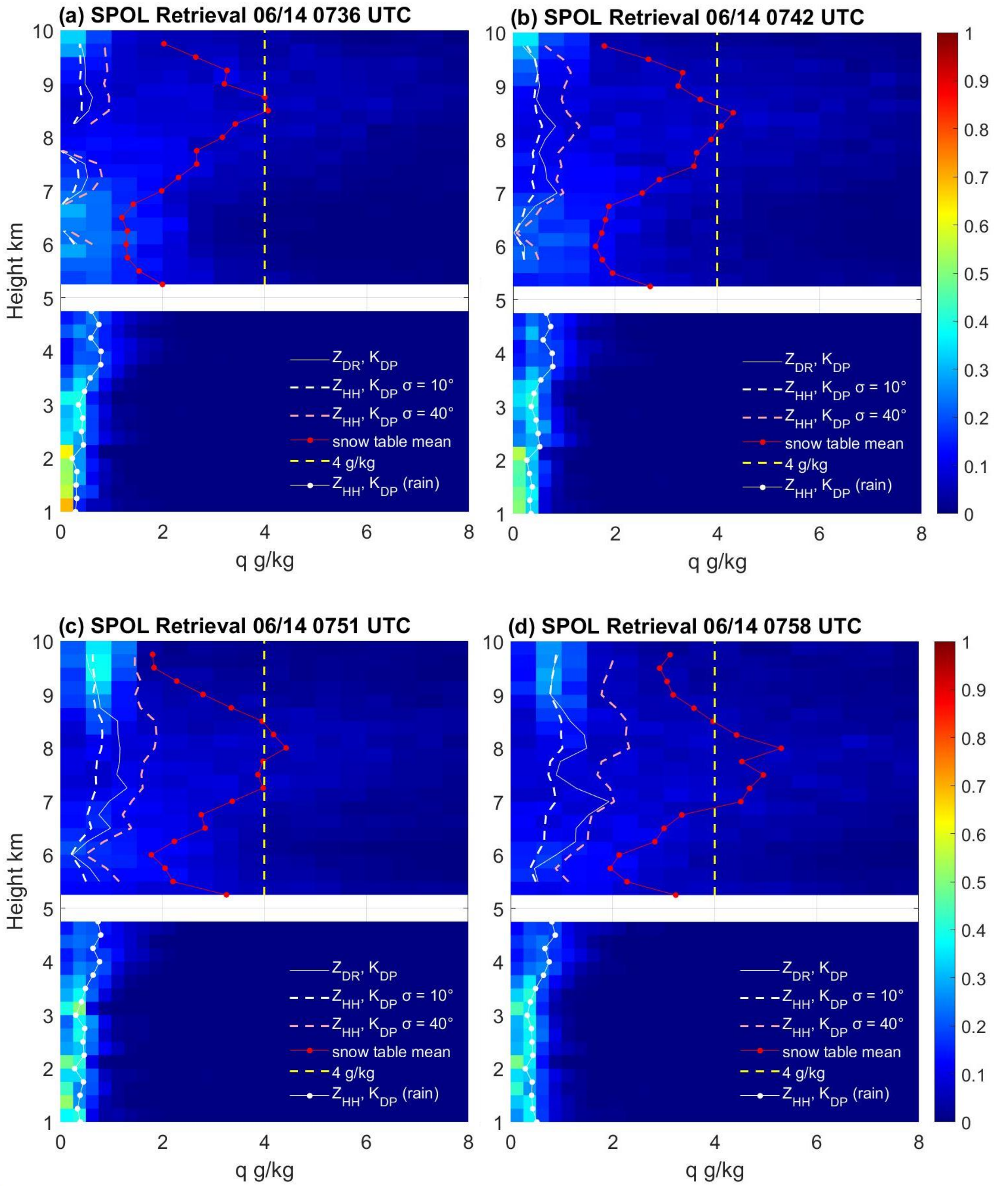

Figure 5.17 The shaded color above 5 km height are CFAD of snow mixing ratio (q) retrieved from SPOL measurements with the snow tables of polarimetric operator, and the red dotted line are average of the snow q. Other lines above 5 km height are averages of snow q from retrieval methods detailed in appendix which derive snow q from Z_{DR} and K_{DP} or Z_{HH} and K_{DP} with σ equals 10° (dendrites or plates) or 40° (snow aggregates). The shaded color below 5 km height are CFAD of rain q, and the white dotted line are average of the rain q (Appendix A.2).

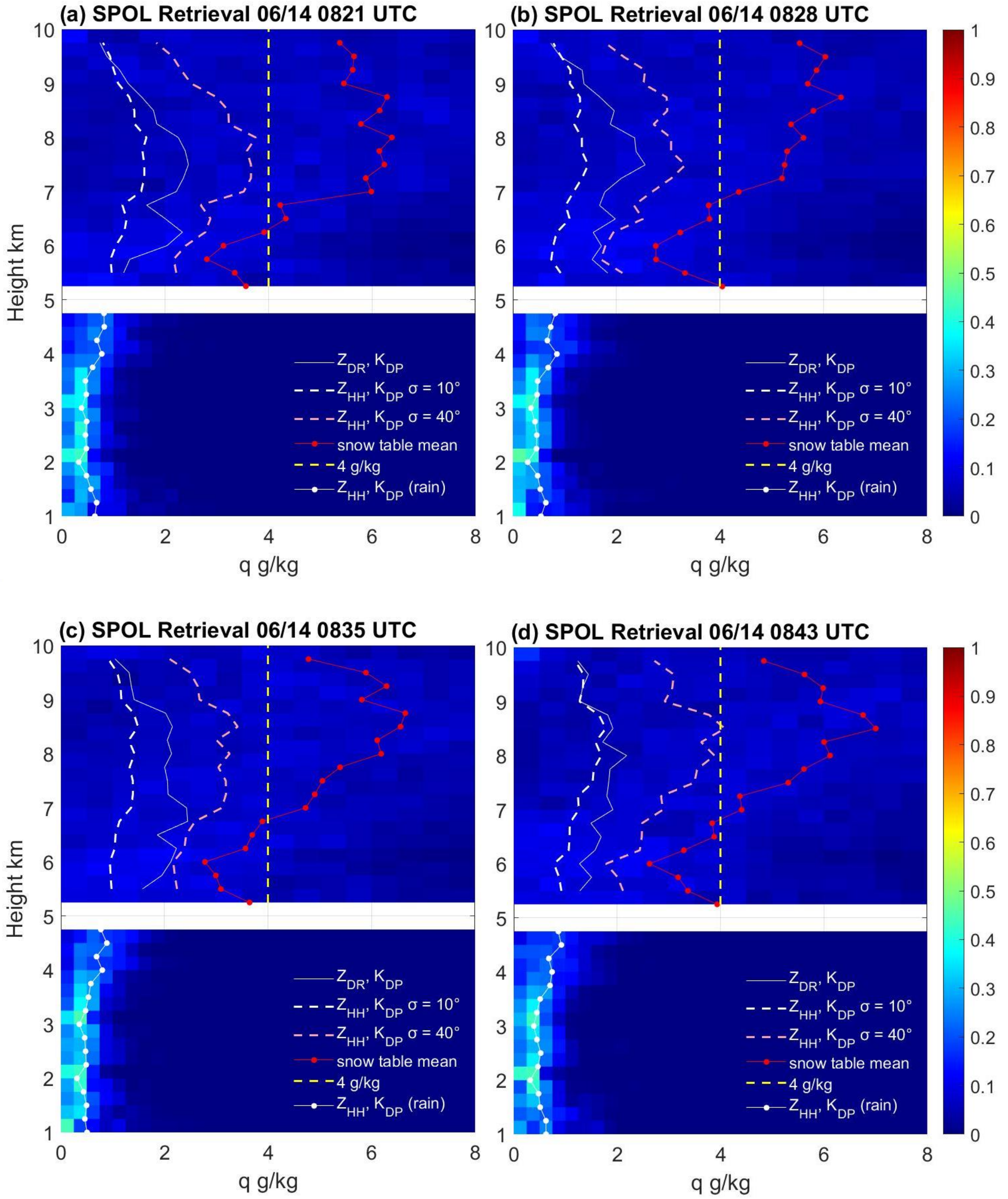

Figure 5.18 Same as Fig. 5.17 but from 0821 to 0843 UTC.

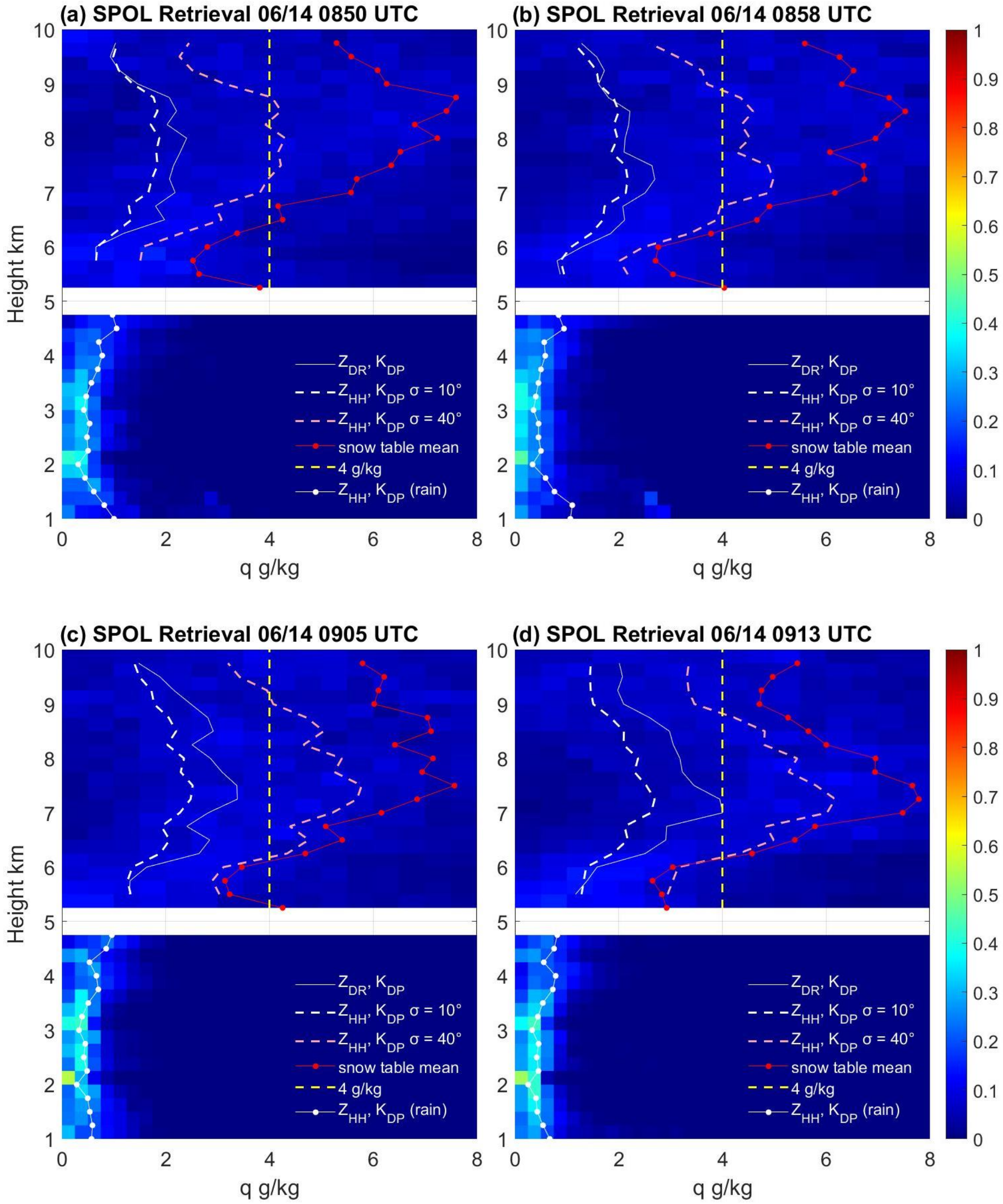

Figure 5.19 Same as Fig. 5.17 but from 0850 to 0913 UTC.

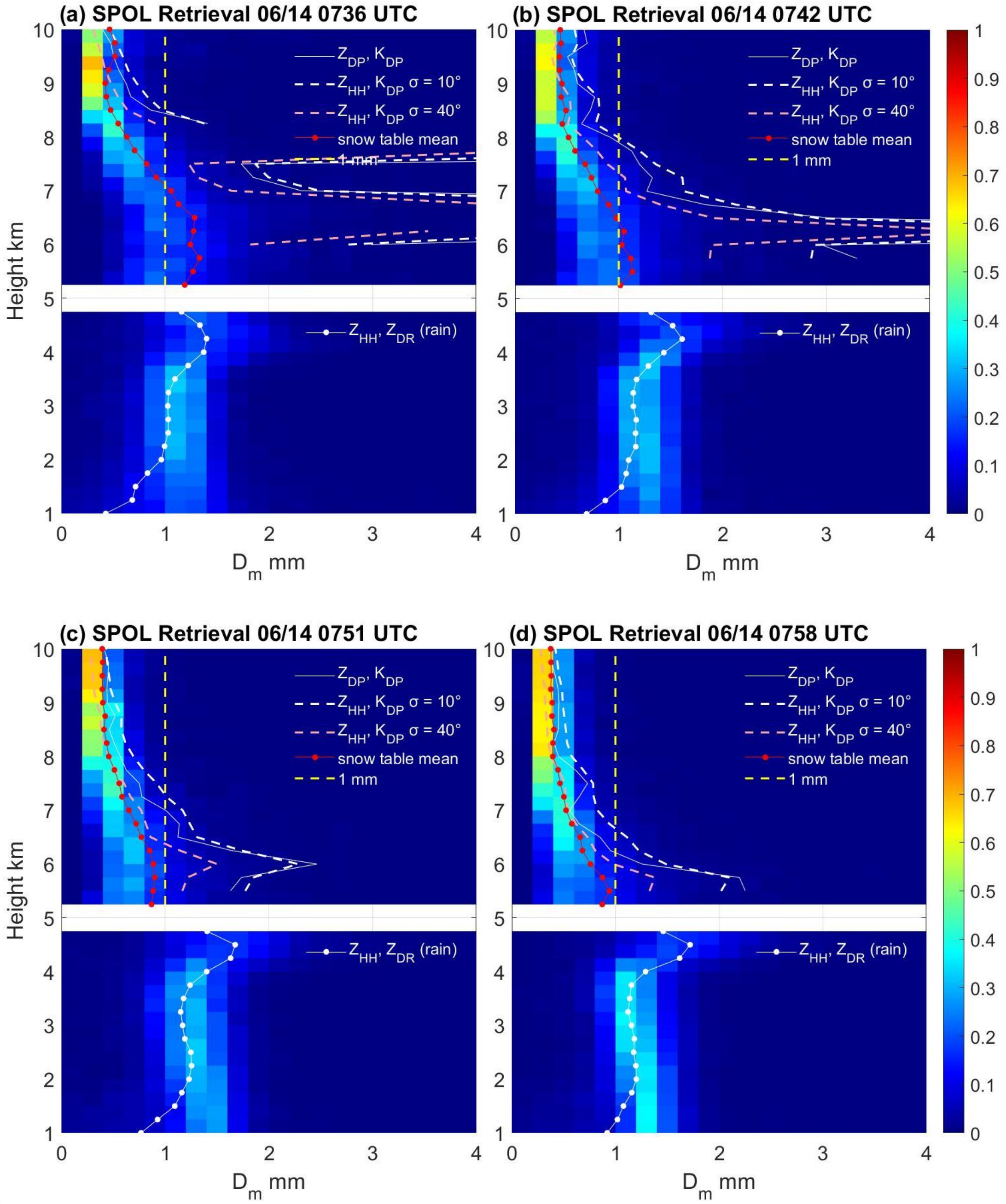

Figure 5.20 The shaded color above 5 km height are CFAD of snow mass weighted diameter (D_m) retrieved from SPOL measurements with the snow tables of polarimetric operator, and the red dotted line are average of the snow D_m. Other lines above 5 km height are averages of snow D_m from retrieval methods detailed in appendix which derive snow D_m from Z_{DP} and K_{DP} or Z_{HH} and K_{DP} with σ equals 10° (dendrites or plates) or 40° (snow aggregates). The shaded color below 5 km height are CFAD of rain D_m, and the white dotted line are average of the rain D_m (Appendix A.2).

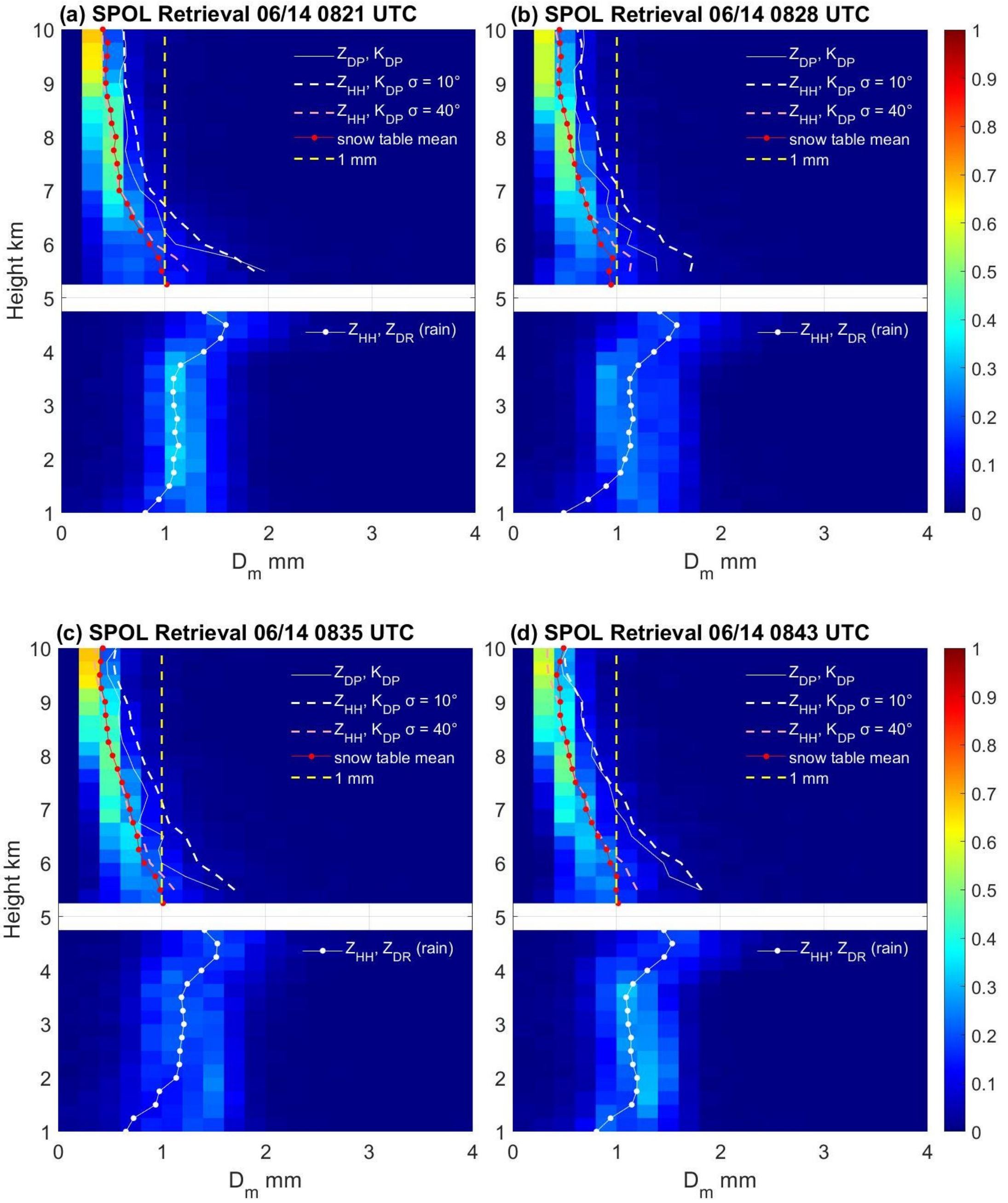

Figure 5.21 Same as Fig. 5.20 but from 0821 to 0843 UTC.

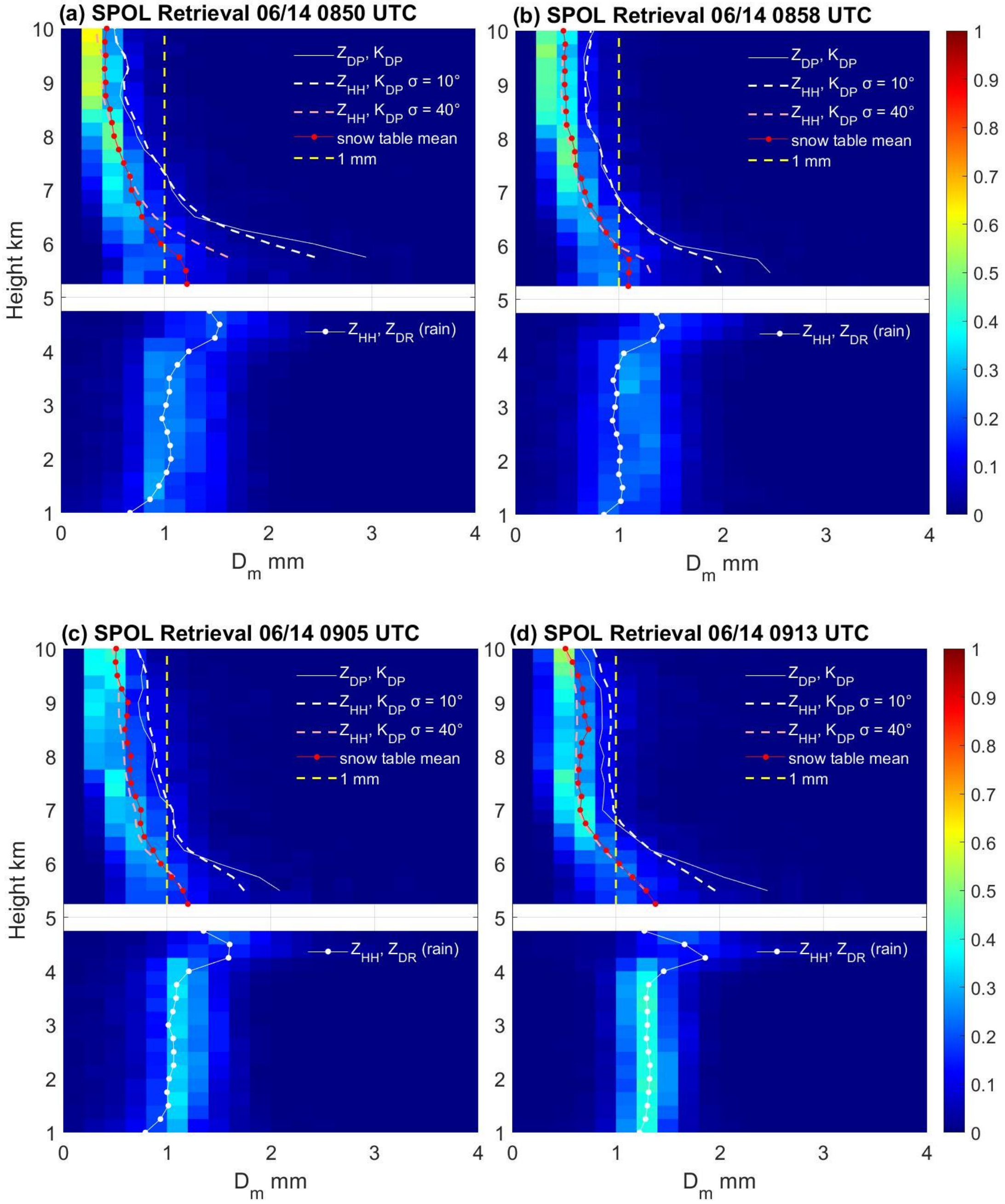

Figure 5.22 Same as Fig. 5.20 but from 0850 to 0913 UTC.

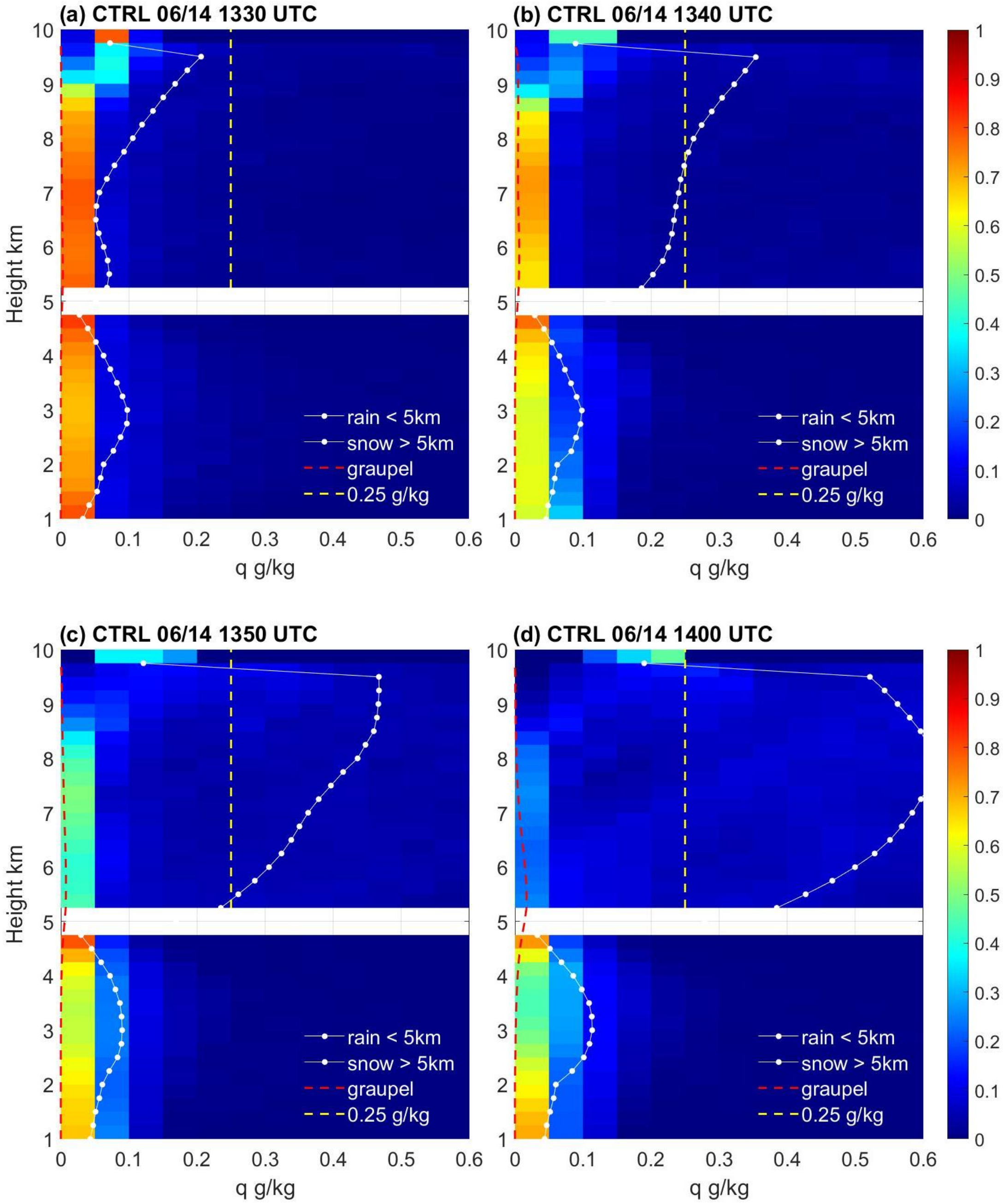

Figure 5.23 Shaded color above (below) 5 km height are CFAD of snow (rain) mixing ratio, and the white dotted line is the average of the snow (rain) mixing ratio. The white dashed line is mixing ratio of graupel.

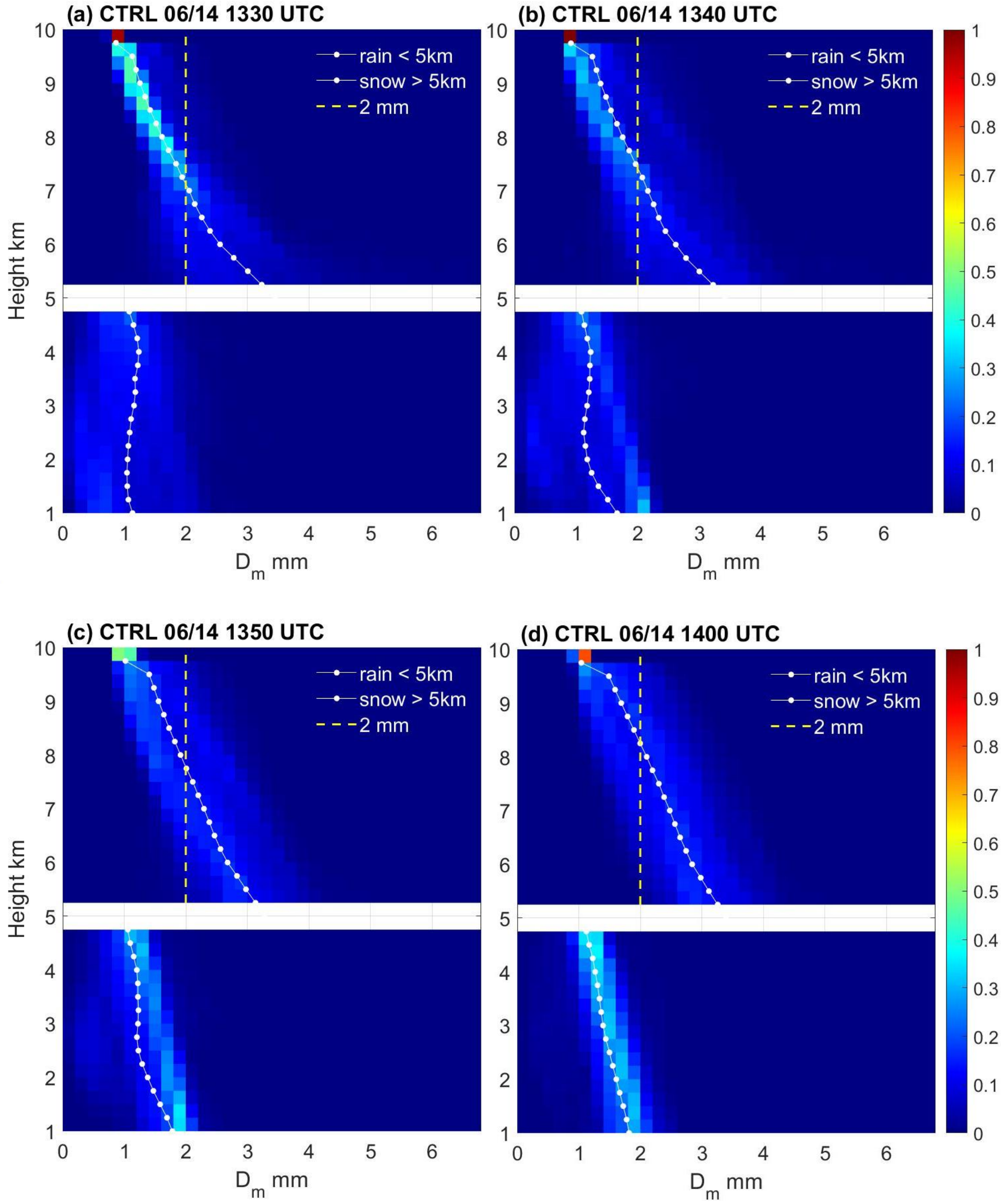

Figure 5.24 Shaded color above (below) 5 km height are CFAD of snow (rain) mass weighted diameter, and the white dotted line is the average of the snow (rain) mass weighted diameter.

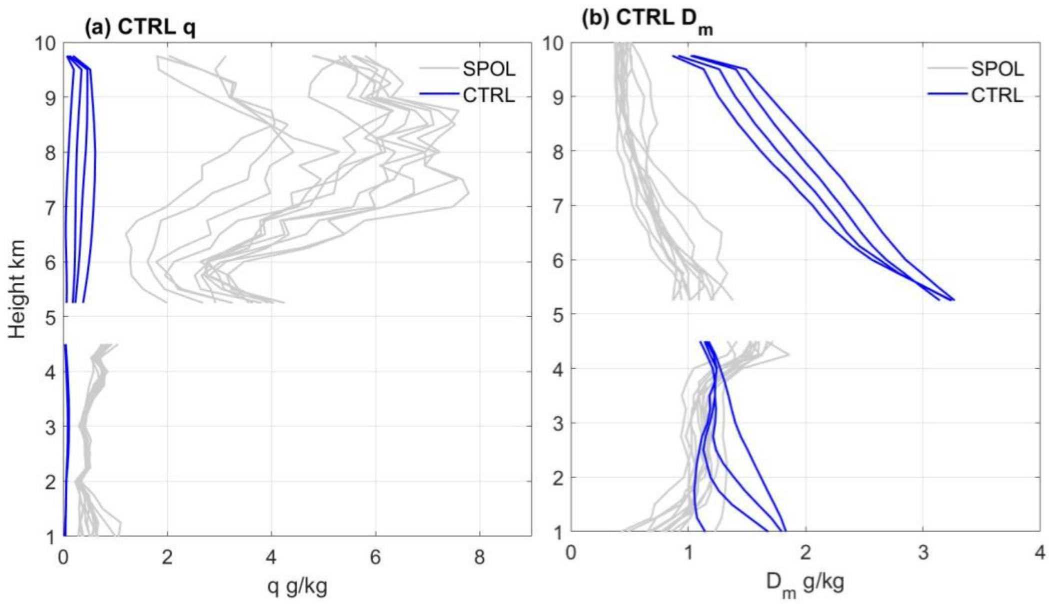

Figure 5.25 Blue solid lines are simulated mixing ratio (left) and mass weighted diameter (right) from 1330 to 1400 UTC. Gray solid lines are retrieved mixing ratio (left) and mass weighted diameter (right) from 0736 to 0913 UTC. For altitude higher (lower) than 5 km, pictures demonstrate mixing ratio and mass weighted diameter of snow (rain).

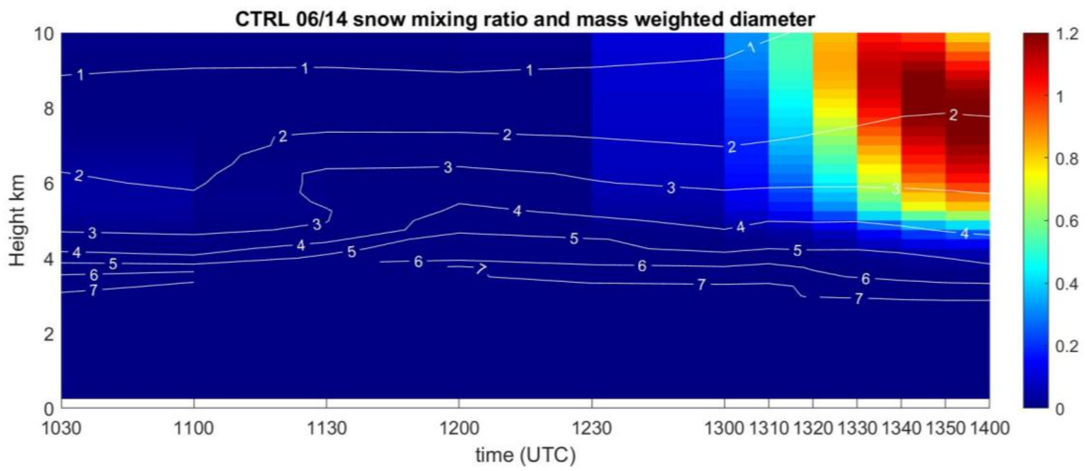

Figure 5.26 White solid lines are simulated mass weighted diameter (mm) of snow. Shaded color are simulated snow mixing ratio (g/kg).

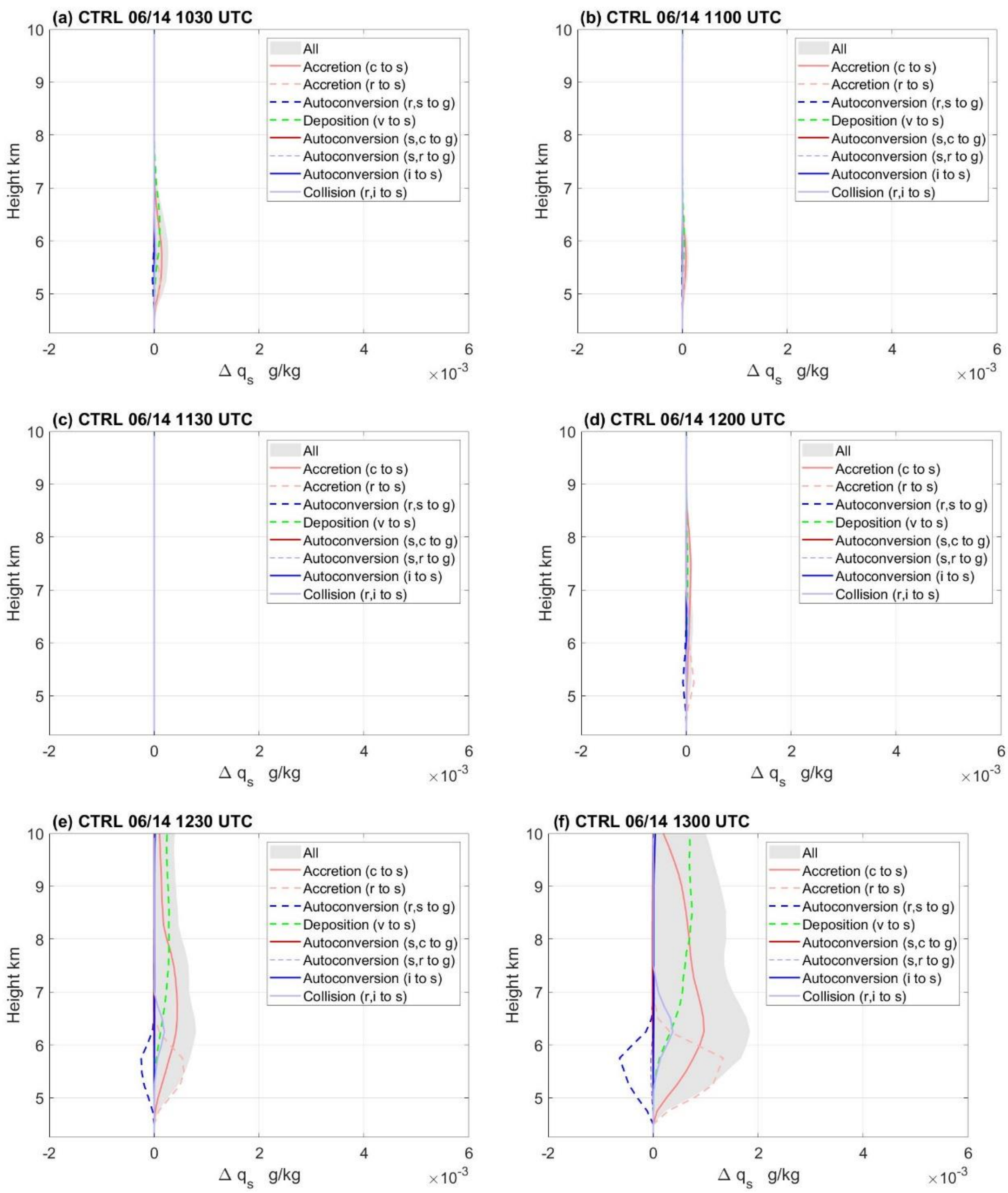

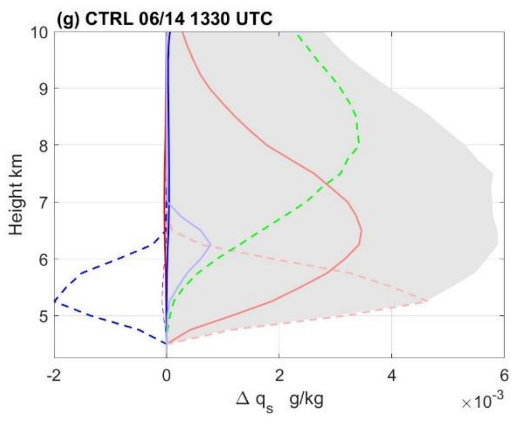

Figure 5.27 The increment of snow mixing ratio from different cold-rain microphysical processes are averaged in altitude. Different lines represent different microphysical processes. The gray area indicates the sum of them.

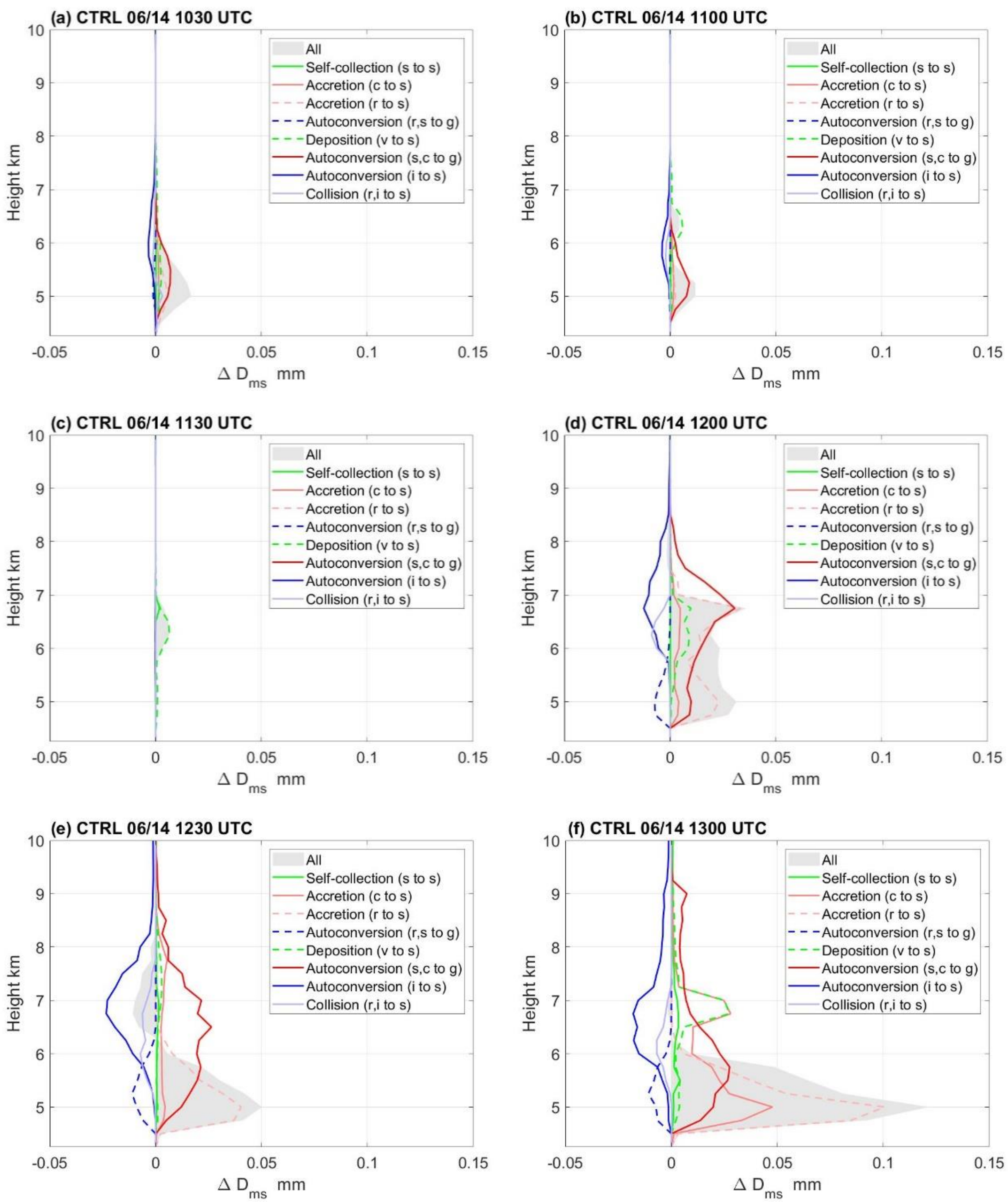

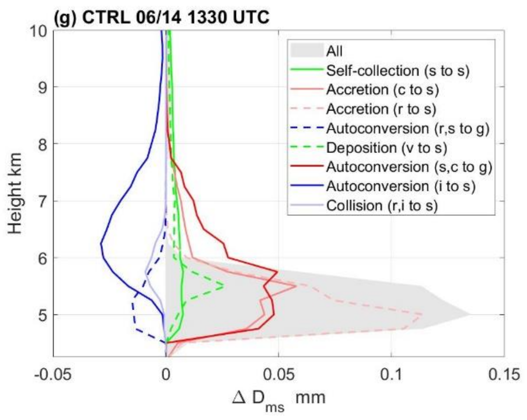

Figure 5.28 The increment of snow D_m from different cold-rain microphysical processes are averaged in altitude. Different lines represent different microphysical processes. The gray area indicates the sum of them.

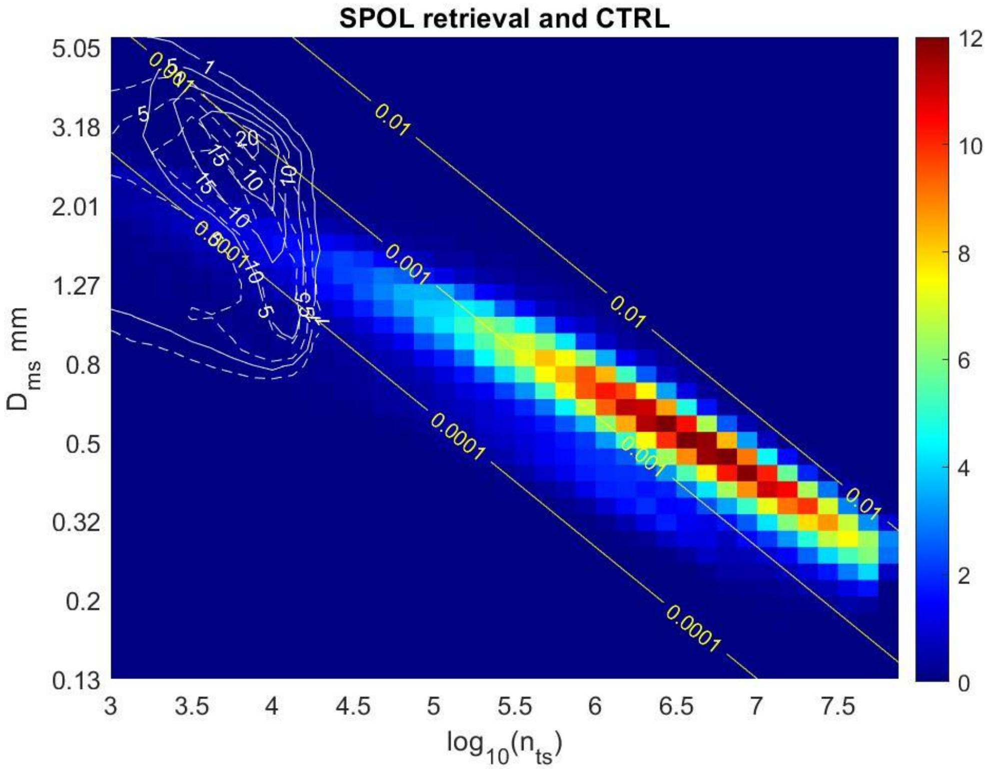

Figure 5.29 The y-axis coordinate is the snow D_m (D_{ms}), and the x-axis coordinate is the snow total number concentration (n_{ts}) in logarithm scale. Under the exponential distribution assumption in DSD, the snow water content only relies on the D_{ms} and n_{ts}. Snow water content equal snow mixing ratio multiplied by dry air density. The tilted yellow lines are the contour of snow water content (0.0001, 0.001, and 0.01kg) and were determined from the coordinated values of D_{ms} and n_{ts}. The shaded color is the distribution (‰) of the SPOL retrieval from 0736 to 0913 UTC above 5 km height in stratiform area. The white solid (dashed) contour is the distribution (‰) of the model simulation from 1330 to 1400 UTC above 5 km height in all (stratiform) area.

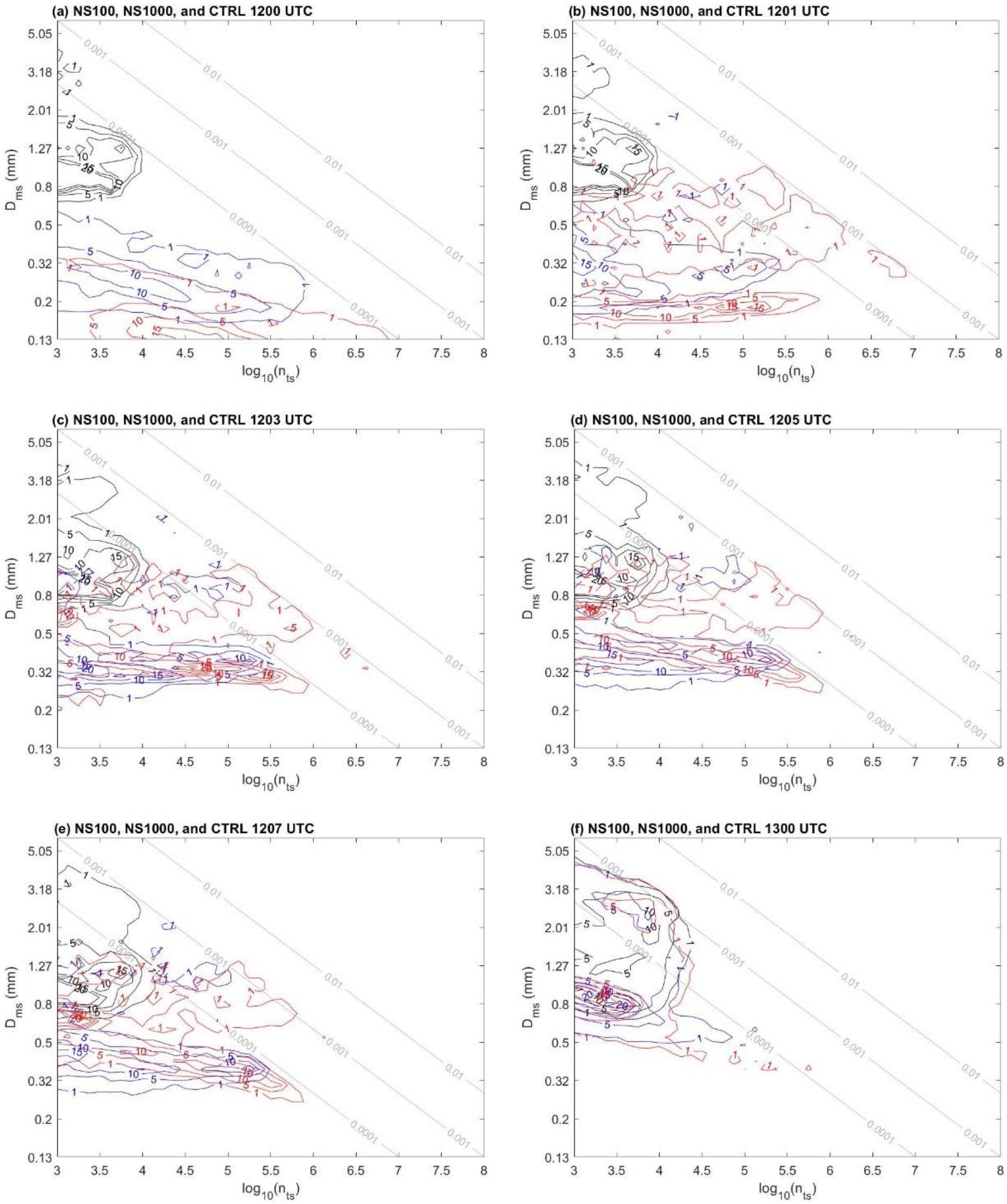

Figure 5.30 The black solid contour is the distribution (‰) of the model simulation above 5 km height in all area. The blue (red) solid contour is the distribution (‰) of the NS100 (NS1000) above 5 km height in all area. The tilted gray contours are the snow mixing ratio. The comparison of snow D_m and n_t distribution between CTRL and sensitive tests (NS100 and NS1000) are demonstrated at 1200, 1201, 1203, 1205, 1207, and 1300 UTC.

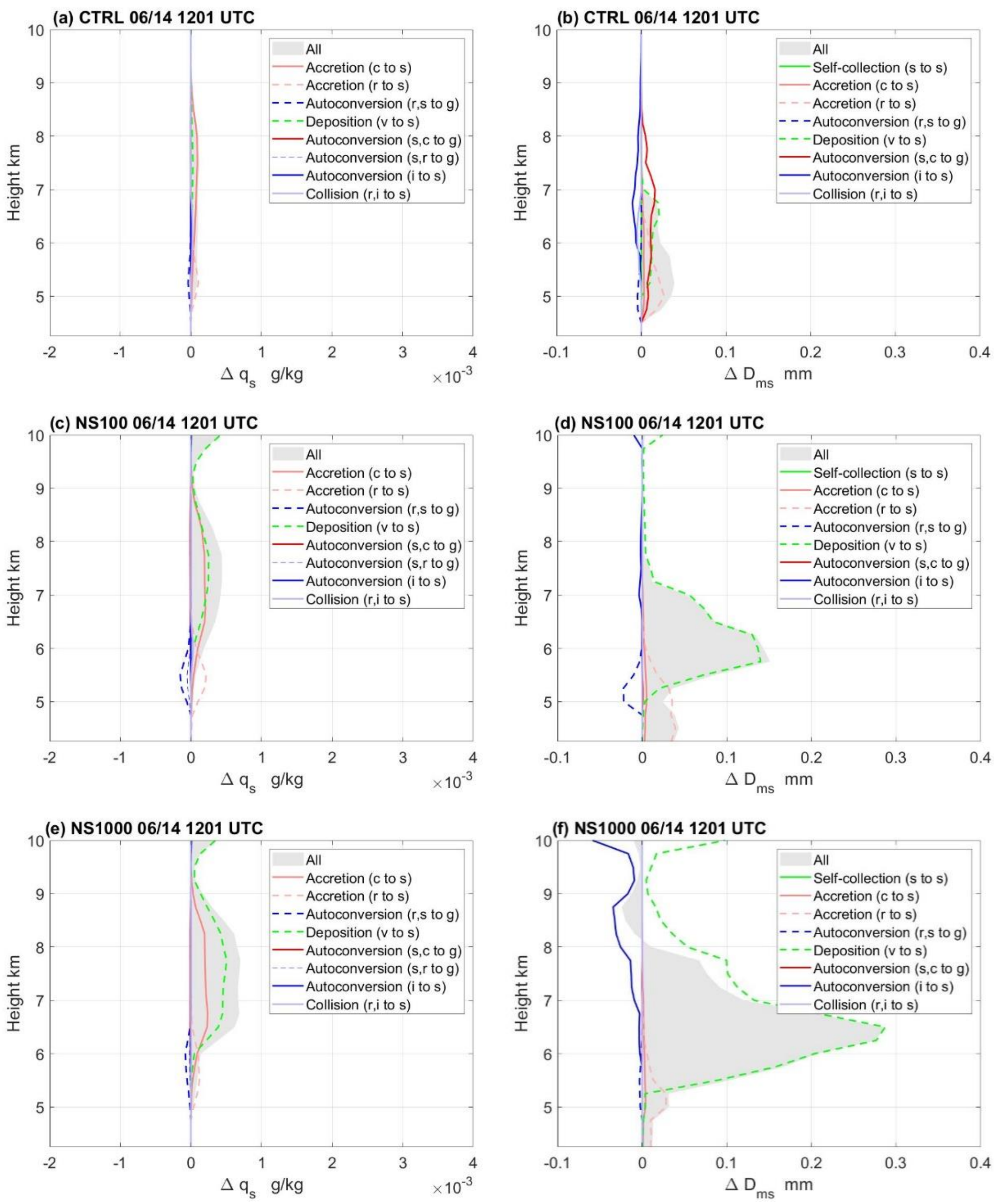

Figure 5.31 The three pictures on the right are the increment of snow D_m from different cold-rain microphysical processes in CTRL (upper right), NS100 (middle right), and NS100 (below right) run. The three pictures on the left are the increment of snow mixing ratio from different cold-rain microphysical processes in CTRL (upper left), NS100 (middle left), and NS100 (below left) run. Different lines represent different microphysical processes. The gray area indicates the sum of these processes.

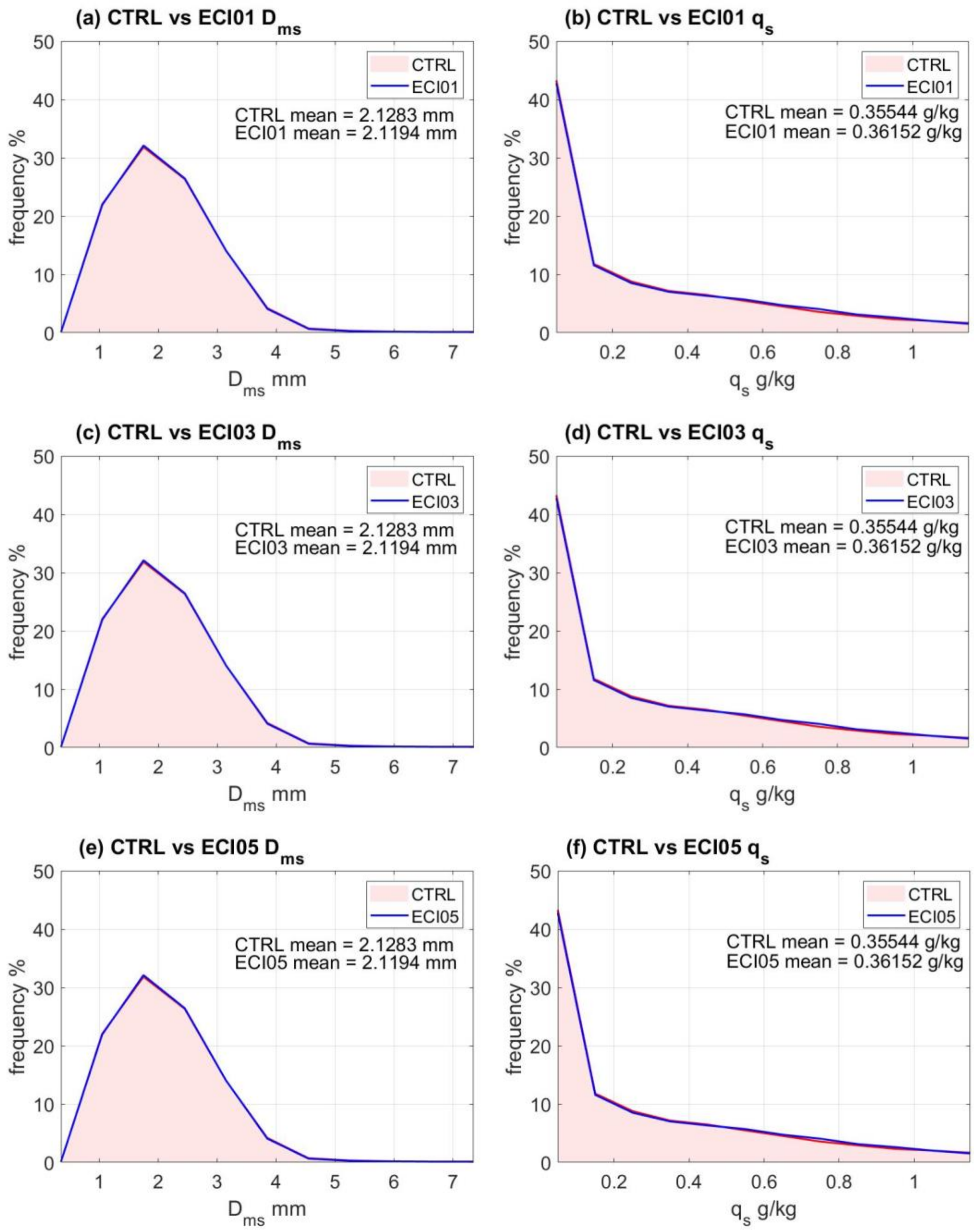

Figure 5.32 The three pictures on the right hand side are the snow mixing ratio comparison between CTRL and ECI01 (upper right), ECI03 (middle right), ECI05 (below right) run. The three pictures on the left hand side are the snow D_m comparison between CTRL and ECI01 (upper left), ECI03 (middle left), ECI05 (below left) run. y-axis coordinate is the frequency of the data above 5 km height. The blue line always indicate the data of CTRL run, while the red line and the pink area are the data of sensitive runs (ECI01, ECI03, and ECI05).

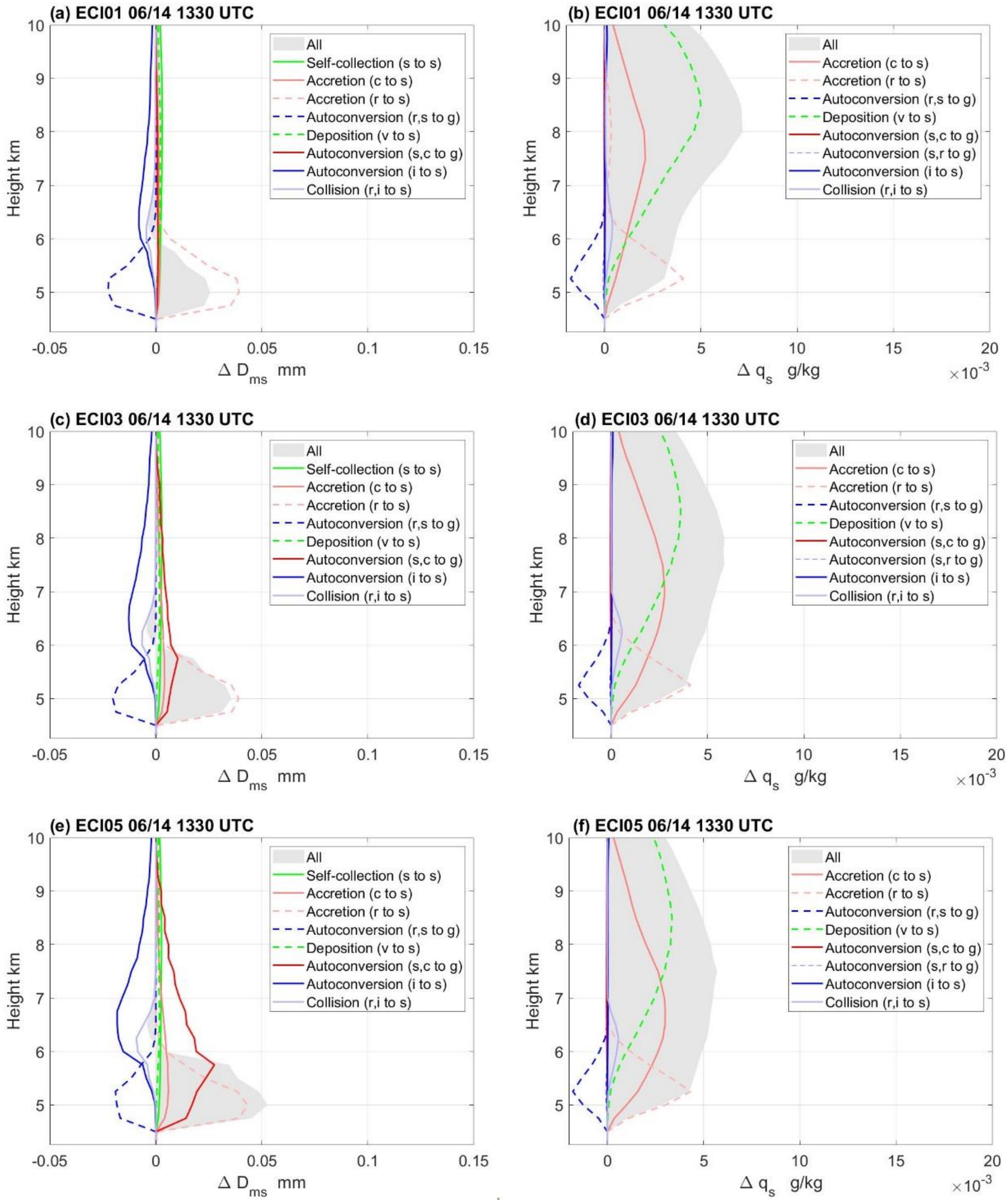

Figure 5.33 The three pictures on the right are the increment of snow mixing ratio from different cold-rain microphysical processes in ECI01 (upper right), ECI03 (middle right), and ECI05 (below right) run. Note that the x-axis ranges of them are different from the ones in Figure 5.27. The three pictures on the left are the increment of snow D_m from different cold-rain microphysical processes in ECI01 (upper left), ECI03 (middle left), and ECI05 (below left) run. Different lines represent different microphysical processes. The gray area indicates the sum of these processes.

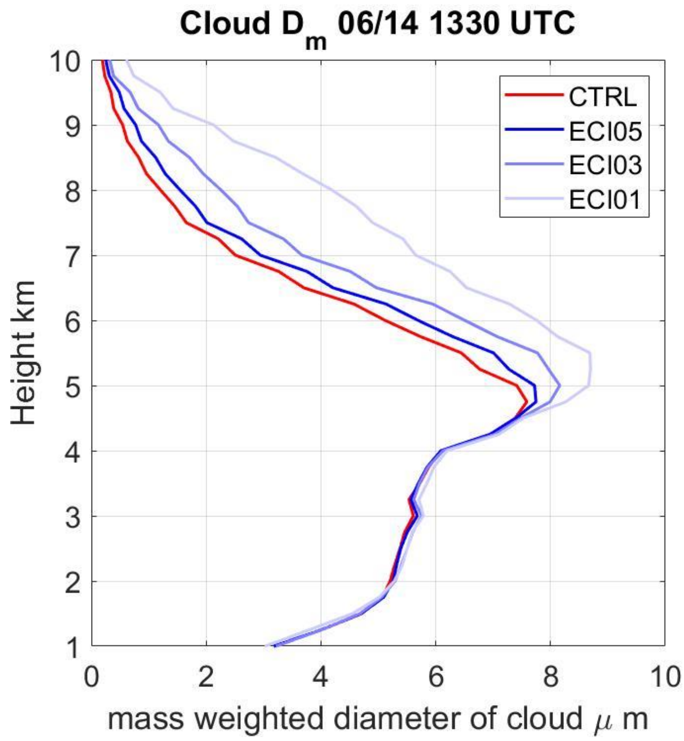

Figure 5.34 The averages of cloud D_m at 1330 UTC of CTRL, ECI05, ECI03, and ECI01 in height.

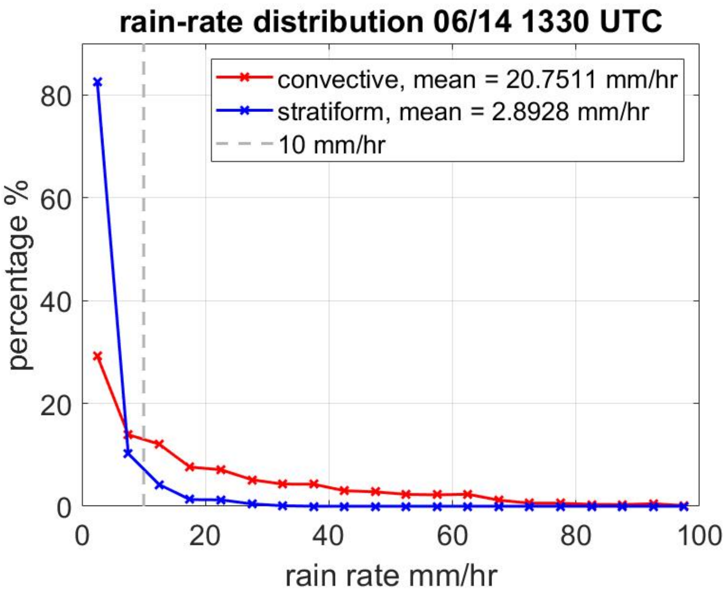

Figure 6.1 The distribution of rain-rate data in stratiform (blue line) and convective (red line) area at 1330UTC. The stratiform and convective area are separated by method based on Z_{HH}. Gray dashed line indicates 10 mm/hr, that is, the common used criteria to distinguish stratiform and convective area.